Transportation Geotechnics 52 (2025) 101549

Contents lists available at ScienceDirect

Transportation Geotechnics

journal homepage: www.elsevier.com/locate/trgeo

Original Article

# Dynamic response of ballasted High-Speed Railways: insights from experimental measurements and 3D nonlinear numerical modelling

José Nuno Varandas [a,*], André Paixão [b], Ángel Tijera [c], Inés Crespo-Chacón [c], José Estaire [c], Eduardo Fortunato [b]

[a] CERIS, Faculdade de Ciências e Tecnologia, Universidade NOVA de Lisboa, 2829-516 Caparica, Portugal
[b] LNEC - National Laboratory for Civil Engineering (LNEC), Av. do Brasil 101, 1700-066 Lisboa, Portugal
[c] CEDEX - Centro de Estudios y Experimentación de Obras Públicas, Laboratorio de Geotecnia, C. de Alfonso XII, 3 & 5, 28014 Madrid, Spain

ARTICLE INFO

*Keywords:*
High-speed railways
Field tests
Ballast dynamics
Numerical modeling
Experimental validation
Railpad stiffness
Track instrumentation

ABSTRACT

High-Speed Railways provide efficient transportation but impose significant dynamic forces on ballasted tracks, accelerating ballast degradation and increasing maintenance demands. This study aims to understand and mitigate these effects by investigating the dynamic behavior of ballasted tracks under high-speed train passages. A field campaign conducted on the Madrid-Barcelona high-speed line involved comprehensive instrumentation of the Brihuega railway segment to capture dynamic responses. These data were used to calibrate and validate an advanced three-dimensional numerical model incorporating nonlinear material properties and Coulomb friction interfaces in an innovative approach. The validated model accurately replicated vertical displacements and revealed that elastic deformations are primarily confined to the railpads and ballast layer, with minimal impact on deeper layers. Non-linear Coulomb friction modeling introduced in the ballast/sub-ballast interface enhanced stress transfer simulations, confirming negligible sliding between these two layers. Decreasing railpad stiffness from 100 to 60 kN/mm reduced ballast stresses by 10 % and improved load distribution, promoting longer track service life, while increasing rail displacements and reducing overall track stiffness by 20 %. This study concludes that railpad stiffness optimization can balance track resilience and degradation mitigation, providing a sustainable approach to infrastructure management. The validated numerical model offers a versatile tool for simulating complex track behaviors, enabling predictions of unmeasurable parameters like stress paths in the track bed. Future work should address long-term loading effects and non-uniform track conditions, advancing track design and maintenance strategies for high-speed rail networks.

## Introduction

High-Speed Rail (HSR) systems are expanding globally, providing efficient and fast transportation, and offering environmental benefits by reducing carbon emissions compared to air and road travel. The increasing speed of rail transport, driven by the growing development of HSR systems in countries such as China and Spain, aims to enhance the attractiveness of this mode of transport, contributing to the sustainability of the global transport system. However, HSR systems require advanced and costly infrastructure, including specialized tracks, signaling systems, and rolling stock. The infrastructure includes both ballasted and ballastless track systems. Although the latter has been gaining popularity due to lower maintenance requirements and better performance at high speeds, ballasted tracks are still the preferred option in many European countries, due to the initial lower construction costs and the well-established methods for track geometry maintenance. Also, Portugal has recently decided to invest in the construction of a dedicated ballasted high-speed railway line, connecting its two major cities, Lisbon and Oporto [56].

A key issue in ballasted HSR systems is that high-speed trains generate significant dynamic forces on the ballast bed, potentially leading to ballast flight, track settlement [9,27] and, therefore, increased degradation [40,43]. These effects result in greater risks for circulation, an increased need for monitoring and maintenance, as well as higher operating costs. Even though the rolling stock and the track superstructure is ready for speeds above 300 km/h, as demonstrated in

---

* Corresponding author.
*E-mail addresses:* jnsf@fct.unl.pt (J.N. Varandas), apaixao@lnec.pt (A. Paixão), angel.tijera@cedex.es (Á. Tijera), ines.crespo@cedex.es (I. Crespo-Chacón), jose.estaire@cedex.es (J. Estaire), efortunato@lnec.pt (E. Fortunato).

https://doi.org/10.1016/j.trgeo.2025.101549
Received 20 December 2024; Received in revised form 16 February 2025; Accepted 14 March 2025

2007 when the TGV set the world record at 574.8 km/h, the current design of ballasted tracks does not support commercial speeds significantly above 300 km/h due to operational and maintenance reasons, among others. Further research exploring the dynamic behavior of ballast under high-speed conditions will thus help in developing solutions that may mitigate these issues and define new commercial speed limit threshold for ballasted HSR.

Ballast is used as a load-bearing drainage material in railway tracks, consisting of high-strength medium to coarse sized aggregates (10–63 mm), free from dust and not prone to cementing action [23]. Ballast behavior has been studied through lab experiments [1,8,9,11,29,33,34,44], field measurements [6,7,13,38], and numerical simulations using different methods, including the Discrete Element Method (DEM) [12,21,31,32,50], the finite element method (FEM) [41,45,55], and lattice models [10]. Laboratory and field studies have shown that after initial dynamic stabilization, when loaded by a single axle load, the ballast layer exhibits a resilient response, essentially recovering, after the train passage, its initial shape. Controlled triaxial tests have also shown that the stress–strain path of ballast under compression loads is non-linear, being the resilient modulus $E_R$ increased with confining pressure, provided there is no significant particle breakage [8,29]. At a microscopic level, when two rock particles are gradually pressed against each other, the contact surface increases, decreasing the rate of change in contact deformation and leading to higher stiffness at higher levels of applied pressure [30].

Despite the development of robust numerical approaches for simulating ballast material and its complex particle behavior using the DEM [2], this method is still limited to small track sections (models extending over only a few sleepers), which strongly restricts its application in simulating HSR systems. Instead, computational studies considering the three-dimensionality of the railway system and potential dynamic effects on the ground from the circulation of high-speed trains have mostly been performed with continuous approaches based either on semi-analytical formulations (e.g. [35,48]) or on the finite element method (e.g. [4,3,20,37]). In these studies, ballast behavior is often simplified by assuming a linear stress–strain relationship, which facilitates model computation but may overlook more complex interactions. While linearizing ballast behavior is generally acceptable for studies focusing on track displacements, it can lead to significant discrepancies in the stress field inside the ballast and sub-ballast layers, because the dependence of ballast stiffness on confining stress is not considered [54]. In some cases, a different source of non-linearity is considered for the deeper layers: the well-known degradation of the soil stiffness with the strain level [25]. This is a key factor in critical speed studies of railway tracks constructed on soft soils.

The study of the dynamic response of HSR systems thus represents a typical soil-structure interaction problem, where studying the complex interactions between ballast and its surrounding elements requires the construction of large-scale three-dimensional models. Additionally, various nonlinear aspects must be considered in detailed analyses, including the nonlinear behavior of ballast, the wheel-rail contact, the sleeper-ballast contact, and sometimes load-deformation state dependency (force non-linearity), among others. Altogether, these aspects pose significant computational challenges in dynamic analyses, which are still impractical with commercial programs, often necessitating the linearization of the problem at the cost of substantial representational accuracy. To address these issues, a three-dimensional continuous representation program based on the finite element method, suitable for large-scale soil-structure interaction nonlinear dynamic analysis, has been continuously developed and coded in MATLAB ® at CERIS and LNEC, referred to as *Pegasus*, which is used in the numerical simulations here presented. For the analyses included in this paper, the program was further developed to include the possibility of Coulomb friction interfaces between sleepers and ballast and between ballast and sub-ballast layers.

This paper first presents the main results from an extensive measurement campaign performed on a ballasted HSR built on high-quality geotechnical ground, which is representative of typical European HSR, with trains passing at approximately 300 km/h. Subsequently, a 3D numerical nonlinear model is developed, using *Pegasus*, and validated by comparison with the field measurements. The validated model is then employed for a more in-depth analysis, focusing on ballast interactions and behavior, considering the nonlinear resilient response of ballast and highlighting critical numerical and behavioral aspects for future studies. Finally, the validated model is used to demonstrate the beneficial effects of reducing railpad stiffness on mitigating ballast layer degradation. This is currently a key issue for railway infrastructure managers, who are exploring the influence of railpad stiffness on maintenance costs.

## Experimental campaign at Brihuega, Spain

### *Description of the case study*

The field measurement campaign was conducted in 2023 by CEDEX on the High-Speed Line (HSL) connecting Madrid to Barcelona, in a section near the village of Brihuega. Over the past two decades, CEDEX has acquired extensive experience in instrumenting and measuring real railway tracks. This has led to the development of a well-established methodology [17,49], used to obtain the measurements presented in this work.

The instrumented section corresponds to a double ballasted track, with unidirectional train circulation in each track. Fig. 1 presents the general cross-section of this HSL in straight track, showing that: (i) the track has a standard gauge of 1435 mm and (ii) the track support layers comprise of ballast, sub-ballast and a form layer. The track superstructure consists of continuous welded 60E1 rails, monoblock concrete sleepers and elastomeric railpads with a nominal vertical stiffness of 100 kN/mm.

The approximate layer profile of the track section was inferred from the spectral analysis of surface waves (SASW). The properties of the different layers and the foundation ground are listed in Table 1, where $\gamma$ is the density, $v_s$ is the shear wave velocity of surface waves, $\nu$ is the Poisson's ratio and $E_0$ is the equivalent elastic modulus for small deformations. In this table, it is seen that: (i) the ballast layer has an average thickness of 0.45 m below the sleeper base; (ii) the sub-ballast and the form layer can be represented as a single uniform layer with a total thickness of 0.75 m; and (iii) the foundation of the track is considerably stiff, with an equivalent elastic modulus approaching or exceeding 1 GPa, increasing with depth.

As seen in results from SASW tests, the instrumented track section is built on high-quality geotechnical ground. The properties of the track superstructure and its foundation, as well as its geometric and structural characteristics, align with the standard design specifications used in typical European HSL. This ensures that the findings of this study are not confined to a single case but instead reflect broader trends relevant to similar HSL.

The results from the Brihuega section presented herein correspond to the passage of a high-speed AVE S-103 train built by Siemens, which is similar to the ICE 3 train operating in Germany (Fig. 2). The train has 32 axles distributed in 16 bogies in 8 cars, running at an approximate speed of 300 km/h on this section [28]. This speed corresponds to the maximum commercial operating speed in the Spanish high-speed network.

### *Instrumentation and data collection from train passages*

Fig. 3 shows the position of the transducers in the instrumented track segment, covering five sleeper spans. Four geophones (range: ± 150 mm/s; sensitivity: 42.9 $\text{V/ms}^{-1}$) were aligned vertically and connected to the rails at locations marked with red rings: three in the outer rail alignment between sleepers 1 and 2 (T12 E), between sleepers 2 and 3

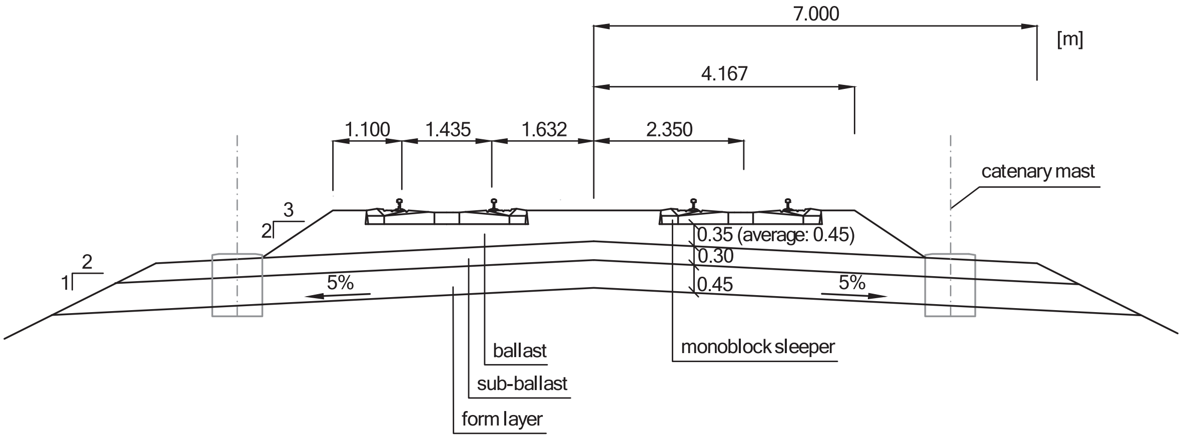

**Fig. 1.** General cross-section of the HSL connecting Madrid to Barcelona.

**Table 1**
Properties of track support layers and track foundation from SASW tests.

| Layer | Thickness (m) | $\gamma$(kN/m$^3$) | $v_s$(m/s) | $\nu$ | $E_0$(MPa) |
|---|---|---|---|---|---|
| Ballast under sleeper base level | 0.45 | 16.5 | 225 | 0.3 | 222 |
| Sub-ballast & form layer | 0.75 | 21.0 | 360 | 0.3 | 722 |
| Embankment | 3.00 | 20.0 | 425 | 0.3 | 958 |
| Soil 1 (Top) | 1.00 | 19.0 | 425 | 0.3 | 910 |
| Soil 2 (Medium) | 5.00 | 19.5 | 650 | 0.3 | 2186 |
| Soil 3 (Bottom) | ∞ | 20.0 | 895 | 0.3 | 4250 |

(T23 E), and between sleepers 3 and 4 (T34 E), and one on the inner rail alignment between sleepers 2 and 3 (T23 I). The instrumented section is shown from two different views in Fig. 4.

The extensometers (comprising strain gauges – resistance: 350 Ω; gauge factor: 2.07; glued to each side of the rail web and connected in a full Wheatstone bridge) are placed at the neutral fiber of the rail, where only shear stresses are considered to exist. They are arranged in pairs, positioned 0.30 m apart, within the same sleeper span (i.e., between two consecutive sleepers) [36].

Four other geophones (range: ± 70 mm/s; sensitivity: 16.4 V/ms$^{-1}$), four uniaxial accelerometers (range: ± 50 g; sensitivity: 5 mV/g), one triaxial accelerometer embedded within a ballast particle (range: ± 30 g; sensitivity: 0.3 mV/g) and four potentiometer displacement transducers (range: ± 2.5 mm; sensitivity: 0.188 V/mm) were mounted at the locations identified in Fig. 3.

## *Data analysis*

### *Wheel loads*

The determination of the instantaneous wheel loads applied by the passage of trains at a given rail section is not a direct measurement but is usually derived from the deformations of the rail measured with strain gauges (Fig. 3) [36]. The wheels loads are in fact obtained by calculating the difference between the shear stresses induced at two points on the rail by the passage of a wheel.

Fig. 5 shows: (i) the loads per wheel measured in the external alignment (E) in the three instrumented spans; (ii) the average values considering the three measurements, and (iii) the corresponding nominal values, made available by ADIF (the Spanish railway infrastructure manager) for this train. It is visible a good correlation between the average measured values and the nominal values, with the average values being on average 12 % lower than the nominal values, with some significant variations. This difference is justified because the nominal loads assume a full load condition. It is also notable that the loads per wheel measured in the three consecutive spans are not equal, generally being found to be higher in section T34 and lower in section T23. With reference to the average values (dotted line), the values measured in section T23 are, on average, 10 % lower, and the values measured in section T34 are, on average, 9 % higher. This very significant variation in the values measured in consecutive sections is probably due not only to precision and measurement errors, but also to rapidly varying dynamic components, possible deviations in railpad stiffness and support conditions in the sleepers, as well as wheel and rail irregularities, as reported in other studies [38].

**Fig. 2.** AVE S-103 train in operation just before arriving the monitored section.

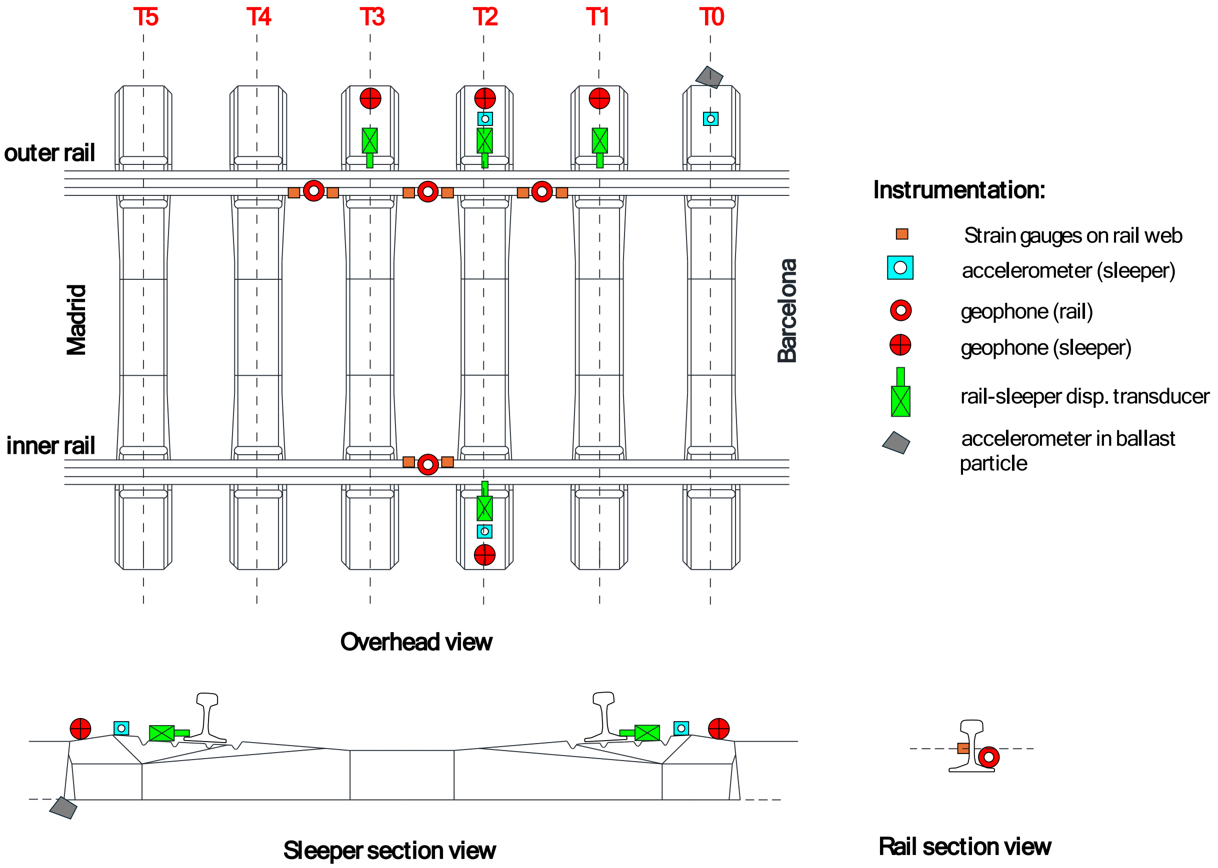

**Fig. 3.** Instrumentation layout in the monitored section.

**Fig. 4.** View of the instrumented track section.

Fig. 6 shows the wheel loads measured at section T23, on both the outer and inner alignments. Once again, significant differences are observed, with the median of these differences being approximately 8 kN, corresponding to 13 % of the wheel load. These differences are also similar to those found in wheel loads measured on adjacent spans of the outer alignment (see Fig. 5). They may be attributed to uneven support conditions of the sleeper along its length, variations in ballast layer thickness due to the transverse drainage inclination of the track bed layers, and/or the dynamic component resulting from transverse vehicle movements, such as hunting motion.

*Rail downward displacements and vertical track stiffness*

The rail vertical displacements (also referred to as deflections) were obtained by time integration of the vertical velocities measured with geophones attached to the rail at the positions shown in Fig. 3. Fig. 7 shows the time-history of rail displacements measured along the outer alignment in the three mid-span sections. These downward displacements result from the deformation of several components: the rail bending, the railpads, the track bed layers, and the subgrade. About 90 % of the measured peak downward rail displacements are in the range 0.31–0.53 mm, with an average value of 0.42 mm. The measured deflections are thus relatively low, even considering the equally low average value of the wheel loads (63 kN).

The downward displacement associated with the passage of the 5th bogie at section T23 is clearly an outlier, probably due to a measurement error. While a wheel flat could theoretically contribute to an anomalous displacement, this is unlikely given the advanced wheel condition monitoring systems in modern high-speed trains such as the AVE S-103. Moreover, the anomaly in Fig. 7 corresponds to two consecutive axles rather than a single wheel impact, suggesting that it is more likely

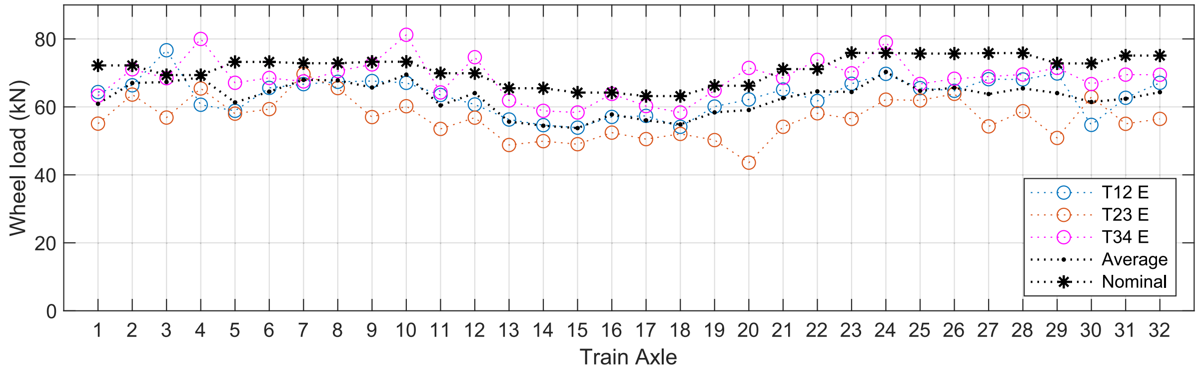

**Fig. 5.** Measured wheel load in exterior alignment, at locations T12, T23 and T34. The average values per train axle and nominal values provided by ADIF are also shown.

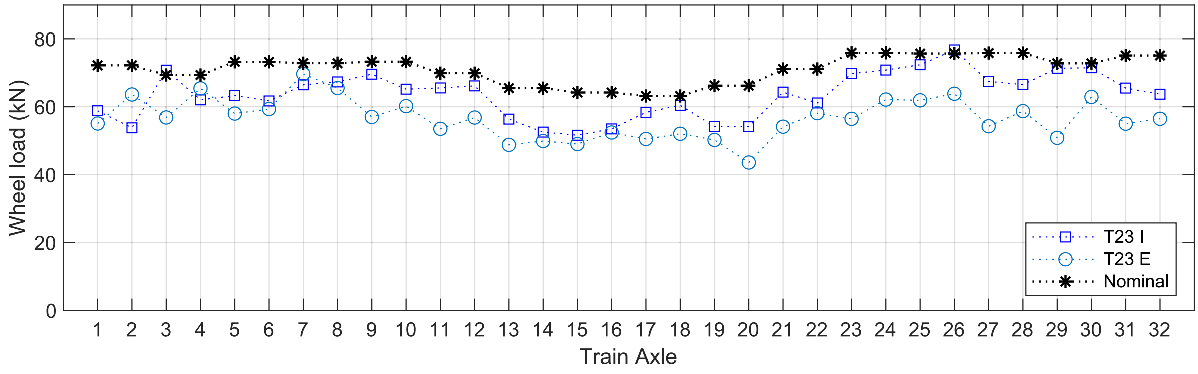

**Fig. 6.** Measured wheel load in section T23, outer (T23 E) and inner (T23 I) alignments.

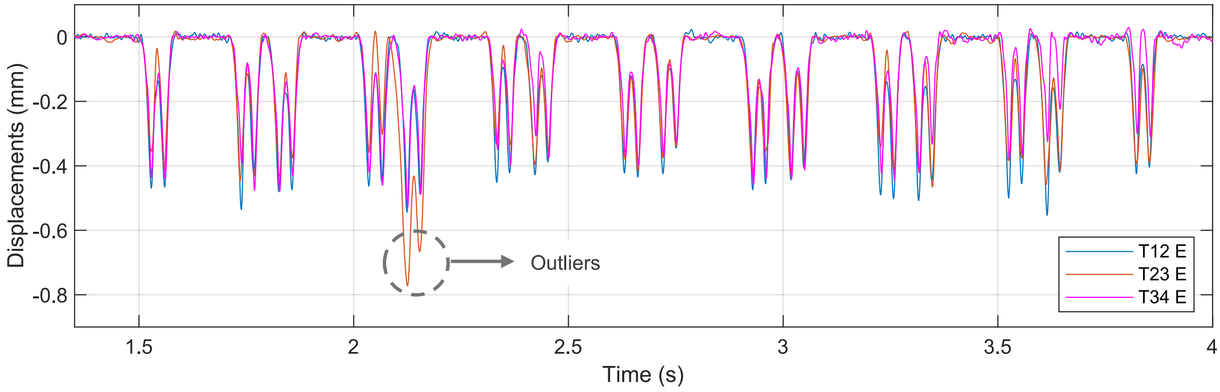

**Fig. 7.** Time-history of measured rail displacements on the outer alignment at the three mid span sections (T12, T23, T34).

caused by transient variations in track support conditions, localized irregularities, or minor integration errors in the geophone signal, rather than a defect in the wheel profile (as e.g. seen in [24]).

For the three instrumented positions in the outer alignment, the corresponding wheel loads (Fig. 5) and the downward peak displacements (inferred from data plotted in Fig. 7) are overlaid on the same graph in Fig. 8, to study if there is a correlation between these two parameters. This correlation shoud indeed exist, as the ratio of the wheel load to the corresponding downward peak displacement represents the vertical track stiffness (see results for this parameter in Fig. 9). It can be observed in Fig. 8 that this correlation is clearly evident, although there are some train axles for which a greater or lesser displacement is not linked with a corresponding greater or lesser wheel load.

The vertical track stiffness, calculated as the ratio between the wheel load and the corresponding downward peak displacement, is presented in Fig. 9, for the three outer alignments. Despite that track sections T12, T23 and T34 are expected to be identical, section T34 appears to be 18 % stiffer than T12 and T23, both exhibiting very similar vertical stiffness. The median value of this parameter for sections T12, T23 and T34 is 139, 144 and 166 kN/mm, respectively. Therefore, it is confirmed that the instrumented track segment has relatively high vertical stiffness, as already expected from the SASW tests presented above.

Fig. 9 also shows that the track stiffness in the considered sections (T12 – T34) appears to significantly depend on the passing axle. This variability does not seem to be related to the track nonlinear response, being likely due to dynamic components caused by multiple factors, such as the random nature of the dynamic response of the system induced by wheel and rail irregularities, different sleeper support conditions, varying railpad stiffnesses and vehicle dynamics, among others. This variability also is not in favor of the validation of a representative

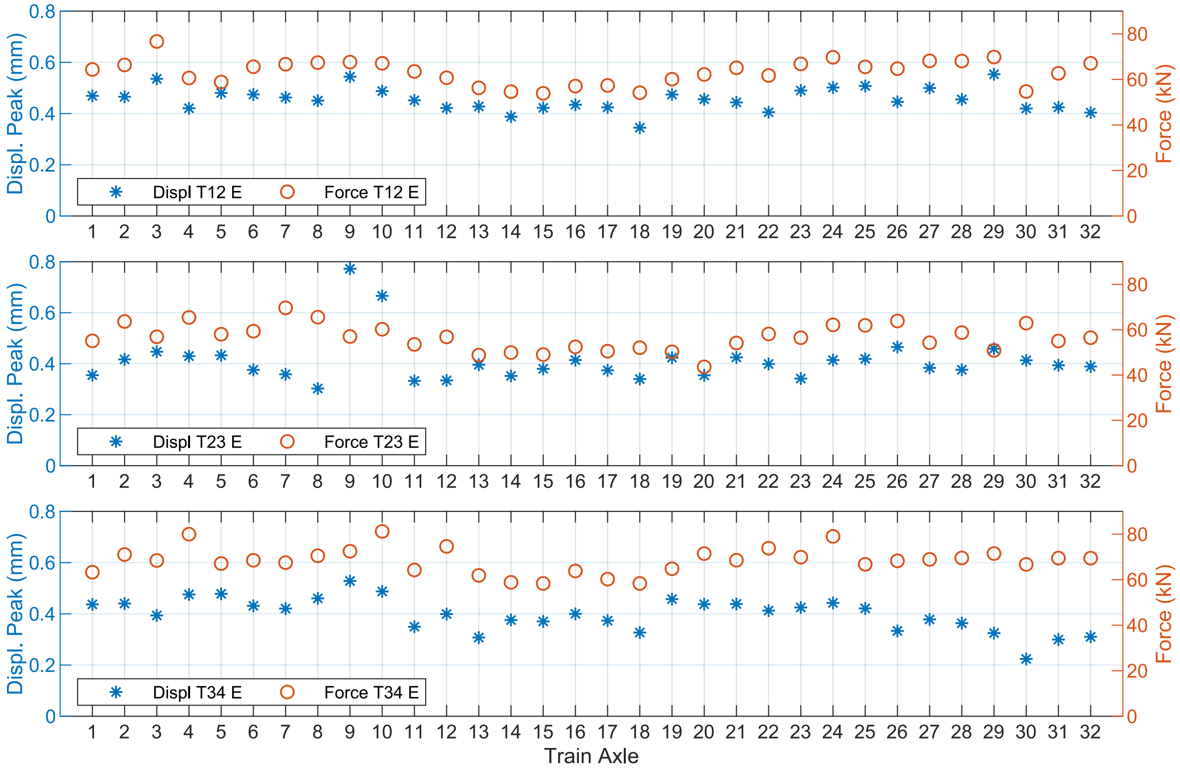

**Fig. 8.** Measured downward rail displacement peaks and wheel forces in the three instrumented positions of the outer alignment.

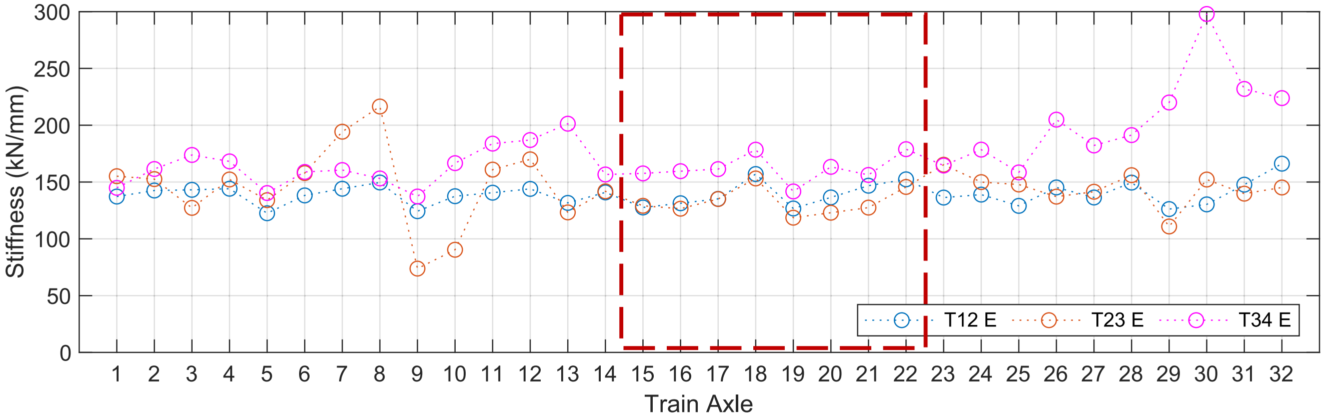

**Fig. 9.** Vertical track stiffness measured in the three instrumented positions of the outer alignment.

numerical model that considers perfectly horizontal rails, and homogeneous support conditions and track stiffness. Examining Fig. 9, it was found that the eight axles 15 to 22, highlighted in the figure with a dashed box, exhibited a comparably more stable track stiffness. For this reason and also aiming at selecting a sufficiently representative portion of the measured response, the measurements from these eight axles – corresponding to four bogies from three consecutive carriages (as shown in Fig. 10) – are those considered for the computational validation process to be presented in section 4.

The rail displacements measured for axles 15 to 22 in the three mid-span sections of the outer alignment are shown in Fig. 11. In this figure, the displacements are synchronized in time (considering the span spacing and the speed of the train) to facilitate comparison and to enable the calculation of an average curve (shown by a dashed dark line), which will be used in the numerical validation process.

Regarding the wheel loads, the average of the values determined in the three mid-span sections for axles 15 to 22 are used in the numerical simulations presented in Section 3. These average values are equal to

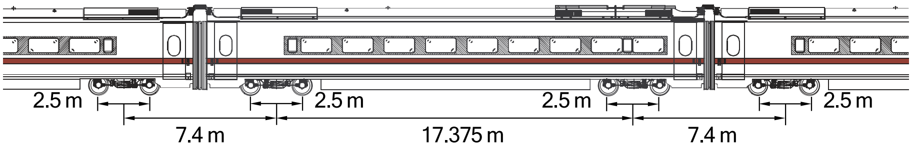

**Fig. 10.** Configuration of axles 15 to 22 of the AVE S-103 train (adapted from [28]).

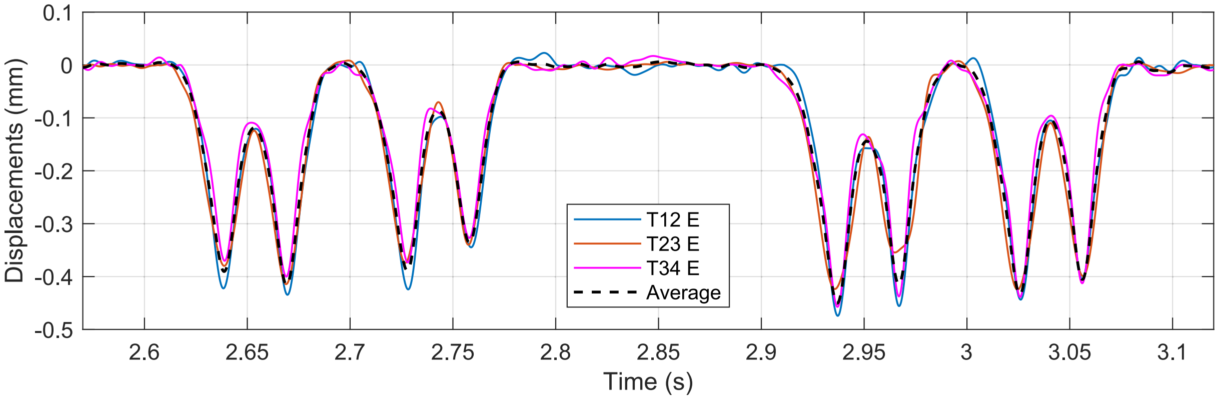

**Fig. 11.** Time history of rail displacements corresponding to axles 15–22, as measured in the three spans of the outer alignment (but time-shifted for overlapping).

53.7, 57.8, 56.0, 54.8, 58.4, 59.1, 62.6 and 64.6 kN, respectively (see Fig. 5).

*Sleeper downward displacements*

The vertical sleeper downward displacements were obtained by time integration of the vertical velocities measured with geophones attached to the sleepers at the positions shown in Fig. 3.

Fig. 12 shows the peak values of the downward displacements reached by the instrumented sleepers in the outer alignment (T1, T2 and T3) during the passage of each train axle, as well as the average value of these three measurements. These downward displacements result from the deformation of the track bed layers and the subgrade. 90 % of the peak values of the downward displacements of the instrumented sleepers are in the range of 0.16 to 0.22 mm, with a median value of 0.19 mm. The results show that the sleeper downward displacement accounts for approximately 45 % of the total rail downward displacement. Regarding the passage of the four train axles chosen for validating the numerical model (axles 15 to 22), the average peak downward displacement ranges from 0.17 to 0.19 mm.

*Railpad vertical deformation*

The vertical deformation of the railpads was directly measured with displacement transducers attached to both the rail and the corresponding sleeper, at the positions shown in Fig. 3.

Fig. 13 shows the peak values of the vertical deformation of the railpads analyzed in the outer alignment (corresponding to the sleepers T1, T2 and T3) during the passage of each train axle, as well as the average value of these three measurements. 90 % of the measured thickness variations of the railpads falls within the range of 0.11 to 0.24 mm, with a median value of 0.19 mm. Although the results for the vertical deformation of the railpads are slightly more dispersed than those of the sleeper downward displacements, they contribute approximately the same amount to the total rail downward displacement (about 45 %). The instrumented railpads undergo an average stiffness reduction ranging from 0.11 to 0.18 mm during the passage of the eight train axles selected to validate the numerical model.

*Sleeper and ballast accelerations*

The accelerations of a ballast particle were measured using an accelerometer embedded within a ballast particle, positioned as shown in Fig. 3. Fig. 14 presents a photo of the instrumented particle, which was placed beneath the edge of sleeper T0. The accelerations of this sleeper were also measured using another accelerometer, directly glued to it, as shown in the left-hand side of Fig. 4.

Fig. 15 presents the measured vertical acceleration signals, on the sleeper and the ballast particle beneath it. A low-pass filter with a cut-off frequency of 175 Hz was applied to these signals, preserving the relevant excitation frequencies of the train travelling at 300 km/h, while removing some high-frequency content due to short-wave irregularities of the rails and wheels (which falls outside the scope of this study). It can be seen that the accelerations on the sleeper are higher than those in the ballast, as expected. The accelerations associated with the leading traction car are also higher than those of the trailing cars. Taking the passage of the central axles 15 to 22 as a reference, the maximum acceleration on the sleeper is around 6.2 m/s$^2$, while on the ballast particle is about 3.0 m/s$^2$. In general, the peak vertical acceleration of the ballast particle immediately under the sleeper is about half the acceleration of the sleeper itself.

## Numerical modeling

### *Description of the program Pegasus*

Program *Pegasus* has been developed over the years in MATLAB® by

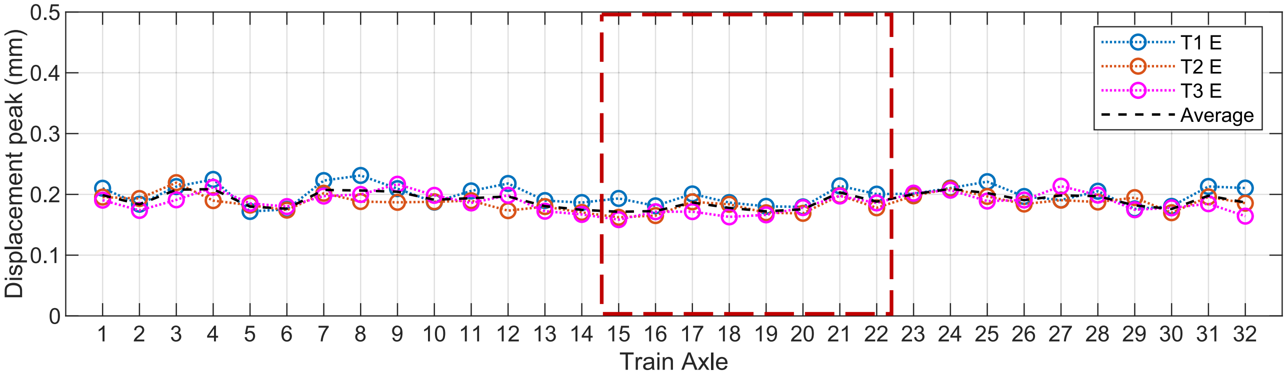

**Fig. 12.** Measured downward sleeper displacement peaks in the three instrumented positions of the outer alignment.

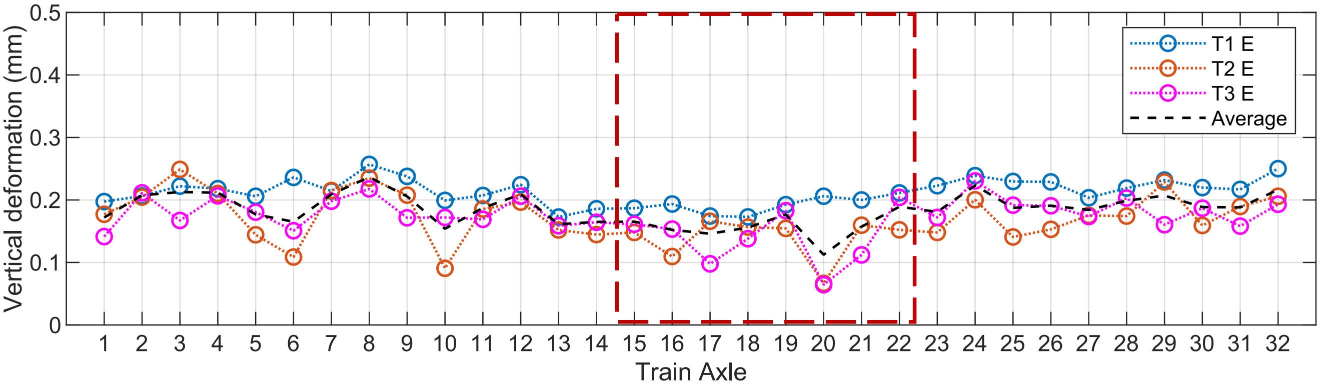

**Fig. 13.** Measured railpads vertical deformation peaks in the outer alignment.

**Fig. 14.** View of the instrumented ballast particle beneath the sleeper edge.

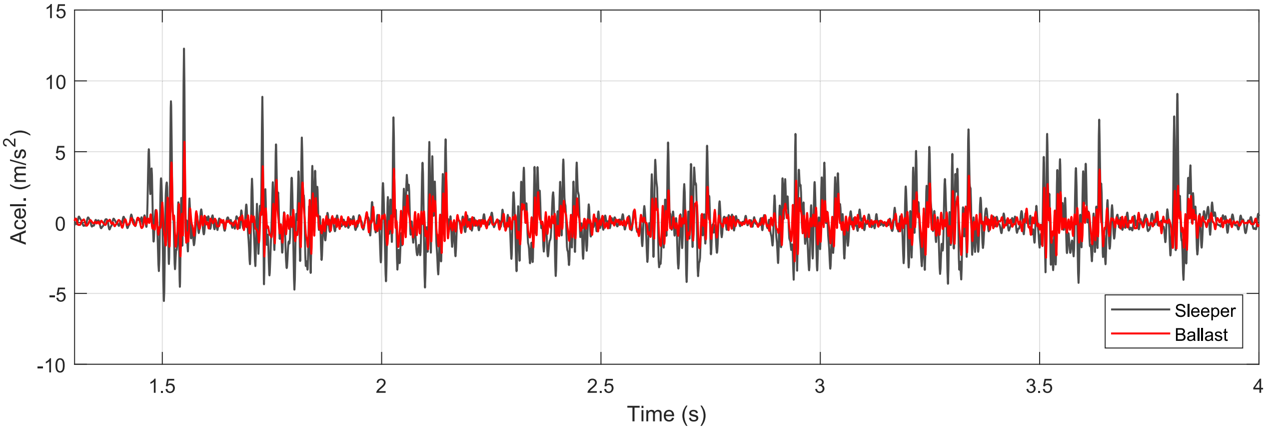

**Fig. 15.** Time-history of measured sleeper and ballast accelerations in vertical direction.

CERIS and LNEC, primarily for the simulation of vertical behavior of railway track systems, considering its three-dimensionality and several important non-linearities. It is based on the finite element method (FEM), and detailed descriptions can be found in previous papers, as [53,55,52].

The complete railway system is composed of several sub-systems with very different mechanical properties and dimensions, which interact through contact forces of a non-linear nature. The *Pegasus* program addresses this diversity by modeling each sub-system separately: (i) the vehicle model (if considered); (ii) the track superstructure (rails, sleepers and railpads); and (iii) the track substructure, which includes the track bed layers (including the ballast layer). In *Pegasus*: the vehicle system can be modeled as an assembly of rigid bodies, springs and dampers; the track superstructure is represented using Euler-Bernoulli beam elements for the rails and the sleepers; and the ballast-substructure system is discretized with low-order, eight-node solid hexahedral elements. Local transmitting boundaries, consisting of visco-elastic dampers, are placed at the lateral boundaries of the model to absorb impinging waves.

The coupled set of equations of motion, one for each sub-system, follows the traditional matrix form for dynamic systems:

$$\begin{cases} \boldsymbol{K}_{\mathrm{v}}\boldsymbol{u}_{\mathrm{v}} + \boldsymbol{C}_{\mathrm{v}}\boldsymbol{v}_{\mathrm{v}} + \boldsymbol{M}_{\mathrm{v}}\boldsymbol{a}_{\mathrm{v}} = \boldsymbol{f}_{\mathrm{g.v}} + \boldsymbol{f}_{\mathrm{c.wr}} \\ \boldsymbol{K}_{\mathrm{t}}\boldsymbol{u}_{\mathrm{t}} + \boldsymbol{C}_{\mathrm{t}}\boldsymbol{v}_{\mathrm{t}} + \boldsymbol{M}_{\mathrm{t}}\boldsymbol{a}_{\mathrm{t}} = \boldsymbol{f}_{\mathrm{g.t}} - \boldsymbol{f}_{\mathrm{c.wr}} + \boldsymbol{f}_{\mathrm{c.sl}} \\ \boldsymbol{K}_{\mathrm{s}}\boldsymbol{u}_{\mathrm{s}} + \boldsymbol{C}_{\mathrm{s}}\boldsymbol{v}_{\mathrm{s}} + \boldsymbol{M}_{\mathrm{s}}\boldsymbol{a}_{\mathrm{s}} = \boldsymbol{f}_{\mathrm{g.s}} - \boldsymbol{f}_{\mathrm{c.sl}} + \boldsymbol{f}_{\mathrm{c.bsb}} \end{cases} \tag{1}$$

where $\boldsymbol{K}$, $\boldsymbol{C}$ and $\boldsymbol{M}$ are the global stiffness, damping and mass matrices of the structural systems; $\boldsymbol{u}$, $\boldsymbol{v}$ and $\boldsymbol{a}$ are, in that order, the vectors of nodal displacements, velocities and accelerations; the subscripts v, t and s refer to the vehicle, track superstructure, and ballast-substructure systems respectively; $\boldsymbol{f}_{\mathrm{g}}$ is the vector of gravity loads; $\boldsymbol{f}_{\mathrm{c.wr}}$ is the vector of the wheel-rail interaction forces, calculated using the non-linear hertzian contact formulation given by $F = k_{\mathrm{c}}\delta^{1.5}$, where $\delta$ is the indentation of the corresponding wheel and $k_{\mathrm{c}}$ is a normal contact stiffness (considered equal to $1.0 \times 10^{8}\ \mathrm{kN/m^{1.5}}$); $\boldsymbol{f}_{\mathrm{c.sl}}$ is the vector of the interaction forces between the sleepers and the ballast; and $\boldsymbol{f}_{\mathrm{c.bsb}}$ is the vector of the interaction forces between the ballast and the sub-ballast when Coulomb friction between these layers is considered. The calculation of the Coulomb friction forces will be addressed specifically in the next section. The damping matrices, denoted by $\boldsymbol{C}$, are determined using the Rayleigh damping approach and represent the material damping of the systems.

In *Pegasus*, the ballast-substructure system and the vehicle system (when considered) are solved using Zhai's explicit integration scheme [57], while the track superstructure system is solved using the implicit Newmark constant acceleration method. This approach significantly reduces computational time compared to using the same integrator for all the three systems [53].

Linear elastic behavior is assumed for all materials and elements, except for the solid elements in the ballast/soil system, which may alternatively follow a pressure-dependent hypo-elastic material law, commonly known as the $k-\theta$ model. In this model, the resilient modulus, $E_{\mathrm{r}}$, of each element at any given time is a function of the sum of the normal stresses ($\theta$), defined as positive in compression, while keeping the Poisson's ratio constant, according to Eq. (2):

$$E_{\mathrm{r}}(t) = \max\left(K_1\left(\frac{\theta(t)}{\theta_0}\right)^{K_2}, E_{\min}\right) \tag{2}$$

The reference stress, $\theta_0$, is set to 100 kPa, and $K_1$ and $K_2$ are model parameters. This nonlinear material model is preferably chosen for the ballast layer, which undergoes the highest stress amplitude variations during train passages. This approach makes that the stiffness matrix $\boldsymbol{K}_{\mathrm{s}}$ is continuously changing during the numerical simulation. To avoid excessive computations in the re-assembly of $\boldsymbol{K}_{\mathrm{s}}$, the elementary stiffness matrices are re-calculated only in $E_{\mathrm{r}}$ modulus changes of 10 kPa (either increasing or decreasing).

To highlight the significance of considering the ballast nonlinear response in dynamic simulation analysis, Fig. 16a presents a longitudinal cut view, showing an example of the instantaneous resilient modulus ($E_{\mathrm{r}}$) distribution in the ballast layer when an axle is positioned above the central sleeper of the three depicted in the figure. It is evident that the resilient modulus is higher under the central sleeper and lower between sleepers and beneath unloaded sleepers. This non-homogeneous distribution closely approximates the force transmission calculated from FEM to the force transmission known from DEM analysis, that is depicted in Fig. 16c. This contrasts with simulations where ballast stiffness is assumed to be homogeneous (in space and time), as shown in Fig. 16b.

### *Coulomb friction interfaces*

The particulate layer of ballast interacts upwards with the sleepers and downwards with the sub-ballast layer. The sleepers are typically made of pre-stressed concrete, and when well-supported on the ballast, contact occurs through a limited number of particles due to the coarse nature of the ballast. However, shared nodes between the sleeper and the ballast in computational models do not accurately represent real track conditions, as it is well-known that contact between the sleeper base and the ballast is often lost, either temporarily during the passage of a high-speed train or due to differential settlements that can lead to the appearance of hanging sleepers [5,15,55]. This is why several numerical simulation approaches have incorporated this important contact nonlinearity.

The sub-ballast, on the other hand, is a layer of well-graded granular material that is usually very well compacted and, therefore, highly stiff. The purpose of this layer is to maintain the integrity of the ballast layer and ensure the reduction of loads to the underlying layers. In the absence of a geotextile to separate these two layers, some level of interpenetration between them, as well as small tangential sliding due to friction, can be assumed. Recent laboratory studies have demonstrated that this interface plays an important role in the long-term cyclic response [11], but further studies are required to fully characterize the mathematical contact relationships at this interface.

The novelty implemented in *Pegasus* and explored in this paper is the inclusion of potential tangential Coulomb friction contact between the sleepers and the ballast (incorporated in $\boldsymbol{f}_{\mathrm{c.sl}}$), as well as between the ballast and the sub-ballast layers (incorporated in $\boldsymbol{f}_{\mathrm{c.bsb}}$). This enables a more realistic stress calculation compared to the shared-node approach.

The interaction forces are calculated at each contacting node (node-to-node contact) of the finite element mesh, requiring nodes duplication. Fig. 17 shows the schematics of the interface force calculation.

The normal force model used in *Pegasus* is the linear spring-dashpot model [14]. In this model, the normal contact force consists of a linear elastic repulsive force and a damping force, that is:

$$F_{\mathrm{n}} = K_{\mathrm{n}}s_{\mathrm{n}} + C_{\mathrm{n}}\dot{s}_{\mathrm{n}} \tag{3}$$

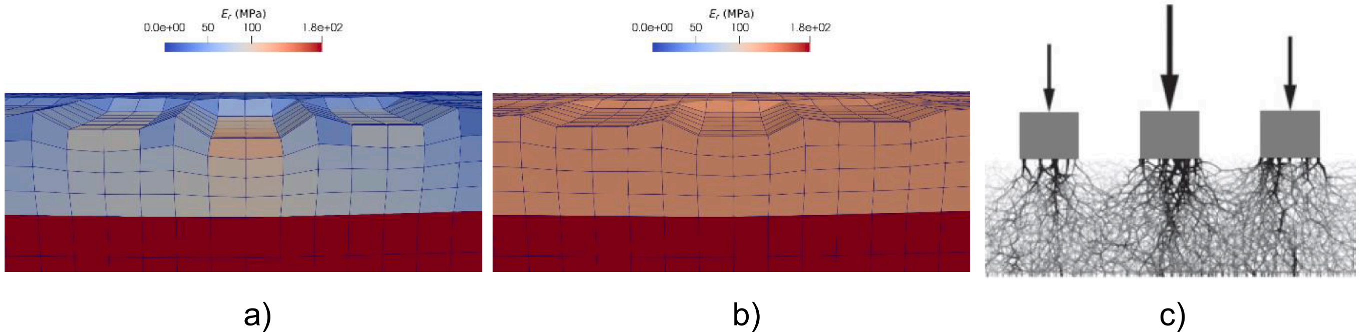

**Fig. 16.** a) Resilient modulus distribution in the ballast layer during an axle passage considering ballast nonlinear resilient response, b) homogeneous distribution of the ballast resilient modulus in equivalent linear analysis, c) force transmission in the ballast layer calculated with DEM (adapted from [12]).

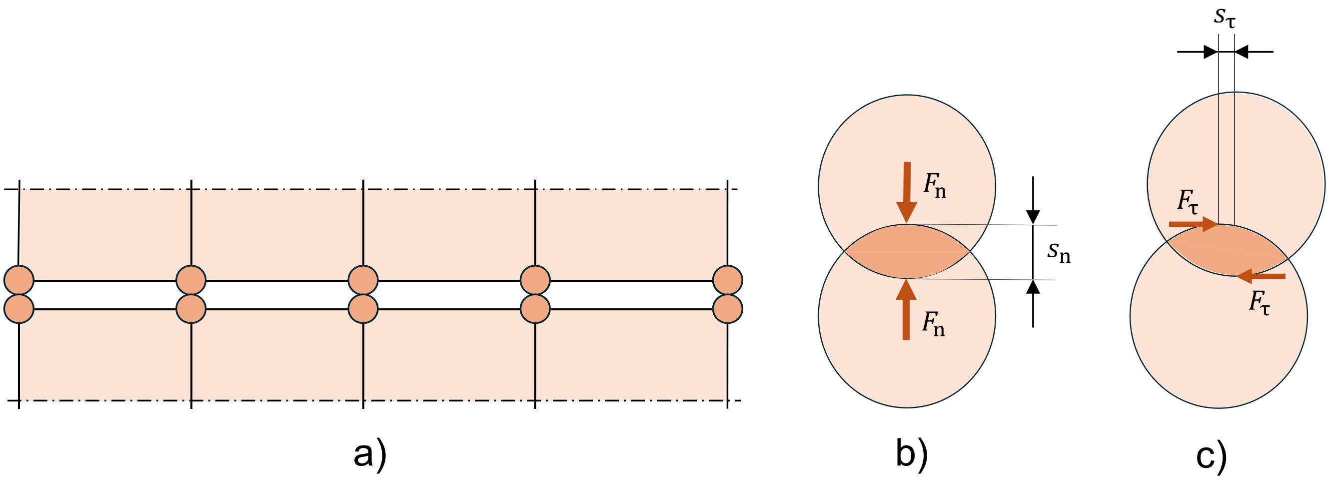

**Fig. 17.** a) Nodes duplication between contacting parts in FEM mesh, b) schematic of the normal force–overlap response, and c) schematic of the tangential force response.

where $K_\mathrm{n}$ is the normal contact stiffness, $C_\mathrm{n}$ is the normal damping coefficient, $s_\mathrm{n}$ is the contact normal overlap and $\dot{s}_\mathrm{n}$ is the time derivative of the contact normal overlap. If not available directly from tests, the value of the normal damping coefficient $C_\mathrm{n}$ is calculated according to [22]:

$$C_\mathrm{n} = 2\eta\sqrt{m^* K_\mathrm{n}} \tag{4}$$

where $\eta$ is the damping coefficient and $m^*$ is the effective mass for the contact, defined as:

$$\frac{1}{m^*} = \frac{1}{m_1} + \frac{1}{m_2} \tag{5}$$

being $m_1$ and $m_2$ the mass of the contacting nodes. The normal contact force is obviously zero for negative $s_\mathrm{n}$.

Regarding the tangential force, *Pegasus* calculates this component using the linear spring Coulomb limit model, which is an elastic-frictional model where the tangential force increases linearly until the Coulomb friction limit is reached. The tangential force in this model is calculated from:

$$F_\tau = \min(|F_{\tau.\mathrm{e}}|, \mu F_\mathrm{n})\frac{F_{\tau.\mathrm{e}}}{|F_{\tau.\mathrm{e}}|} \tag{6}$$

being $\mu$ the friction coefficient and $F_{\tau.\mathrm{e}}$ the elastic tangential force, calculated from:

$$F_{\tau.\mathrm{e}} = K_\tau s_\tau \tag{7}$$

where $K_\tau$ is the tangential stiffness and $s_\tau$ the tangential relative displacement.

### *Initial state calculation*

The drawbacks of considering nonlinear contacts, such as Coulomb friction, in the numerical implementation are that (i) it forces a sequential calculation process that includes determining first the

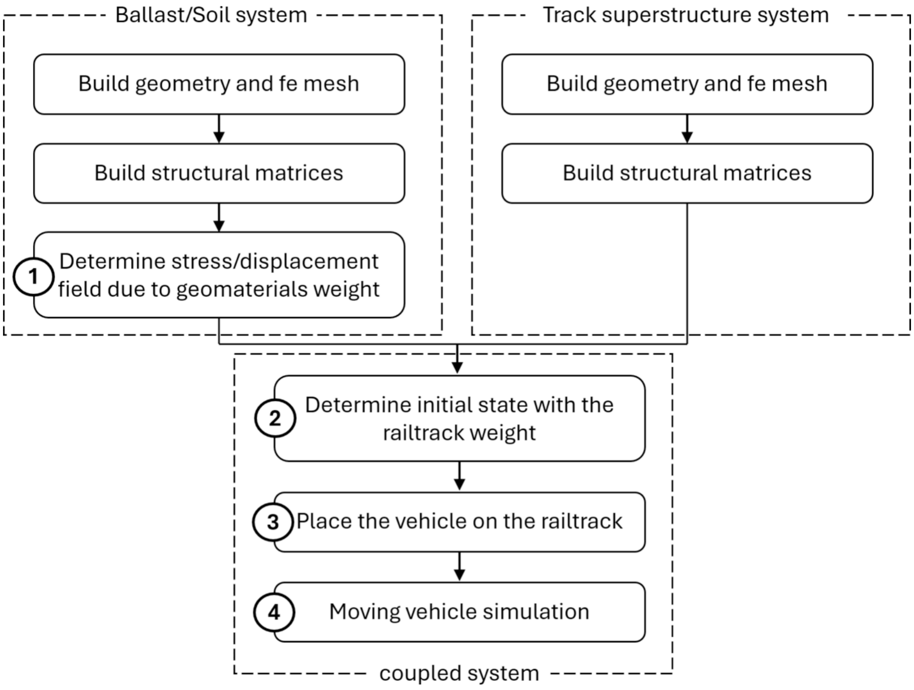

**Fig. 18.** Simulation steps in *Pegasus*.

gravitational stress-displacement field, and (ii) it limits the solution methods to those able to handle singular stiffness matrices and nonlinearity. Fig. 18 shows the calculation steps in *Pegasus*, which includes four simulation stages indicated as **1**–**4**.

When interface contact is defined between ballast and sub-ballast, the corresponding static gravitational stress/displacement fields (simulation **1**) are calculated using the same dynamic explicit solver considered for the train passage simulations (simulation **4**). Otherwise, the static stress/displacement field due to the geomaterials weight can be determined alternatively using the static Conjugate Gradient Method for linear systems, which is usually faster. Simulations **2** and **3** are performed with a dynamic mixed implicit-explicit solver to incorporate the track superstructure system and the corresponding sleeper-ballast nonlinear contact.

When calculating a static stress/displacement field using a dynamic solution method, it is necessary to define a total calculation time long enough to allow for the almost complete dissipation of any oscillatory motion that may arise. This total time depends on the natural frequencies of the system and the material damping. A greater material damping would result in a shorter total time due to a rapid attenuation of the oscillating motion. However, care must be taken because directly increasing the damping matrix may also lead to an undesirable reduction in the required time-step, producing the opposite effect. To avoid this, a method is proposed and implemented in *Pegasus*.

In dynamic simulations performed to calculate intrinsic static fields (simulation steps **1** and **2** identified in Fig. 18), the material damping of the ballast/soil system, $\boldsymbol{C}_s$, is artificially increased by a factor of 1.25, affecting only its diagonal terms. This proposed value of 1.25 was determined through a trial-and-error procedure. Fig. 19 shows an example of the corresponding obtained results, considering both the original damping matrix and the augmented damping matrix with a factor of 1.25 applied to the diagonal terms. The reduction in the required total calculation time is evident, decreasing from 1.5 s to 0.4 s, while the time-step required by the explicit solver remained the same. This corresponds to a direct computation time reduction of 0.4/1.5.

### *Model calibration*

This section presents the model developed to represent the Brihuega railway section, calibrated using site characterization data (e.g., SASW), and known properties of the track components (e.g., nominal values of the railpad properties). Fig. 20 shows the cross-section of the FEM mesh that was initially built to represent the track section detailed in Fig. 1. It is worth noting that the ballast above the bottom level of the sleepers is not explicitly considered in the modeling (though its weight is), nor is the drainage inclination of the form layers. The embankment and Soil 1 layers were treated as a single uniform layer due to their very similar estimated moduli (see results from SASW tests in Table 1).

The track superstructure consists of continuously welded UIC60E1 rails, monoblock concrete sleepers (with simplified dimensions 2.6 × 0.3 × 0.19, in m, and a weight of 322 kg each), and railpads with a vertical stiffness of 100 kN/mm and a damping constant of 9.6 kNs/m [39]. In the model, standard material properties were used for the rails and sleepers, while the properties for the geomaterials beneath the ballast layer were derived from the SASW test results (Table 2). The solid hexahedral elements represent the top three layers. The bottom layer referred to as Soil 2 is modeled as a 2D visco-elastic foundation placed at the bottom of the FEM mesh (with formulae provided, e.g., in [51]. The deeper Soil 3 layer was not included in the model because the deformation caused by train passages is expected to be negligible within this stiffer soil layer. The material damping was set to 3 % for frequencies 10 Hz and 220 Hz, following the Rayleigh damping approach.

The elastic parameters assumed for the ballast $k-\theta$ model were $K_1 = 120$ MPa, $K_2 = 0.6$, and$E_{\min} = 15$ MPa. These values were inferred from large-scale triaxial tests performed at the University of Nottingham [8]. Fig. 21 shows the variation of the ballast resilient modulus with the mean stress $p$. In this figure, it is seen that $E_r$ equals 58 MPa at $p = 10$ kPa, while $E_r$ increases to 203 MPa at $p = 80$ kPa.

Preliminary dynamic analyses were performed to validate the minimum size of the FEM mesh and the required model extension of the model in both the lateral and longitudinal directions. This was done by achieving a stationary eigen-field independent of the model dimensions and the maximum train speed considered. Additional analyses also allowed concluding that a symmetry simplification was feasible, as the displacements in the ballast and sub-ballast layers at identical locations to the left- or the right-hand sides of the track centerline (depicted in Fig. 20) were basically coincident. This simplification allowed for the FEM model to be reduced by half, significantly reducing the required computational time.

Fig. 22 presents a 3D view of the final FEM model considering the symmetrical simplification. The model spans 79 sleepers in length (47.7 m), and 6.65 m in the transverse direction (representing 13.30 m without symmetry). The model comprises around 388 000 degrees-of-freedom and 117 000 solid elements, of which 9656 present nonlinear material behavior. The required time-step in the simulation with the moving train was $5.6 \times 10^{-5}$ s. The computation time on a Intel Core i5-9600 K CPU for a train speed of 300 km/h, accounting for all steps described in Fig. 18, is approximately 1.8 h per simulated second when ballast nonlinearity is considered. This may be reduced to around 30 min per simulated second if the ballast is modelled with linear behavior.

For the sleeper-ballast contact, the considered contact parameters were $K_n = 1 \times 10^7$ kN/m$^3$, $K_\tau = 1 \times 10^6$ kN/m$^3$, $C_n = 6.7$ kN/ms$^{-1}$/m$^2$ and $\mu = 0.43$. The friction coefficient ($\mu$) for the sleeper-ballast contact was derived from friction resistance tests performed in CEDEX that pointed to a friction angle of $\phi' = 35^\circ$ for this interface [42] and using the relation: $\mu = \tan(2/3\phi')$. Regarding the ballast/sub-ballast interface,

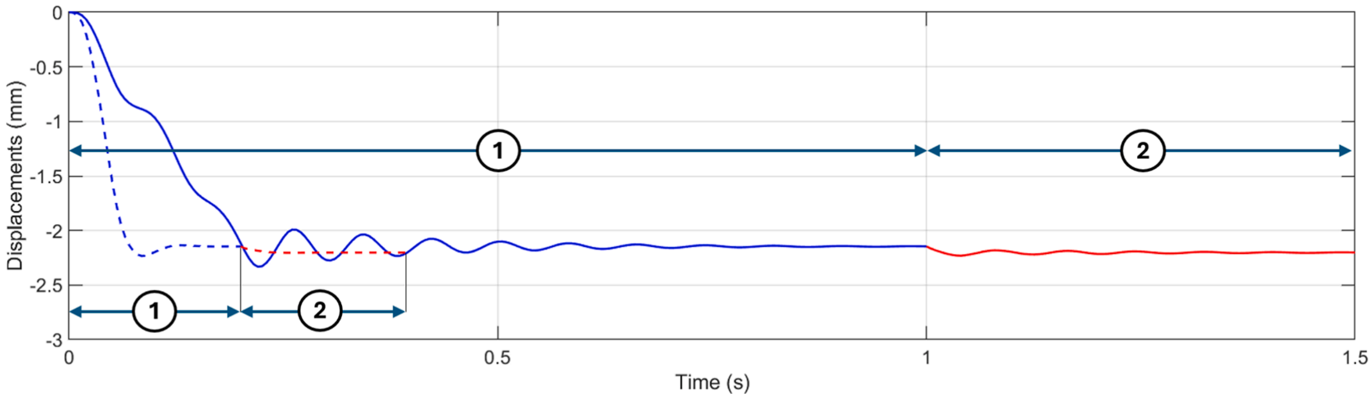

**Fig. 19.** Simulation time required to calculate the static stress/displacement field using a dynamic solution method, considering both the original damping matrix (solid line) and the augmented damping matrix (dashed line).

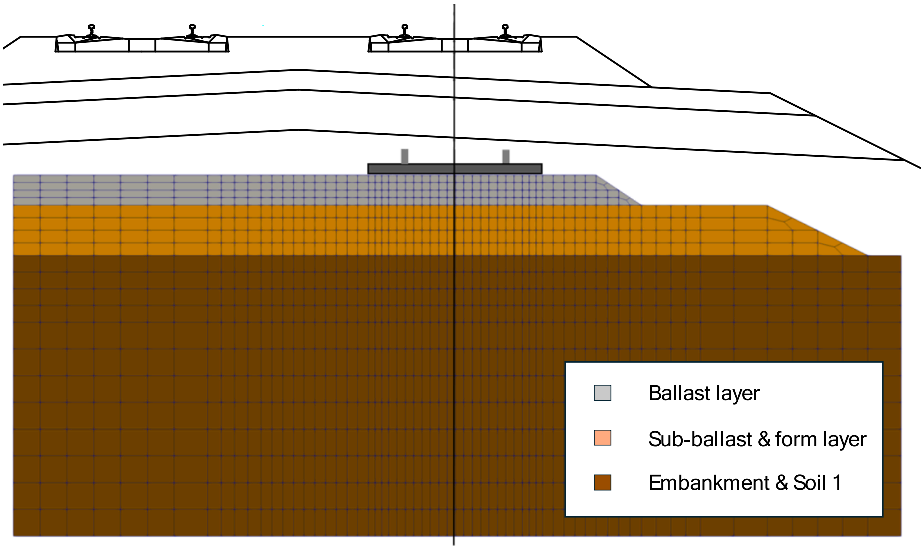

**Fig. 20.** Cross-section of the initial model built to evaluate potential symmetry simplification. AutoCAD drawing above and corresponding FEM mesh below.

**Table 2**
Properties of the materials of the track and its substructure assumed in the model (Notes: * – Equivalent density value calculated to obtain a total weight of 322 kg for each sleeper; $^{+}$ – This layer is represented as an equivalent visco-elastic plane foundation).

| Track component or geomaterial | Height | Density | Resilient modulus | Poisson's ratio |
|---|---|---|---|---|
| | [m] | $\rho_i$ [kg/m$^3$] | $E_{r,i}$ [MPa] | $\nu_i$ [-] |
| Rails | – | 7860 | $210 \times 10^3$ | 0.35 |
| Sleepers | 0.19 | 2170* | $30 \times 10^3$ | 0.25 |
| Ballast | 0.45 | 1650 | (variable) | 0.30 |
| Sub-ballast & form layer | 0.75 | 2100 | 722 | 0.30 |
| Embankment and Soil 1 | 4.00 | 2200 | 958 | 0.30 |
| Soil 2 $^{+}$ | 5.00 | 1950 | 2186 | 0.30 |

the used contact parameters were $K_n = 1.5 \times 10^7$ kN/m$^3$, $K_\tau = 1.5 \times 10^6$ kN/m$^3$, $\eta = 0.025$ and $\mu = 0.65$. The friction coefficient ($\mu$) was derived from triaxial and direct shear tests conducted on samples of ballast and sub-ballast that pointed to a friction angle of $\phi' = 50^\circ$ [11,18]. The stiffness coefficients were set at considerably high values to minimize interpenetration between contacting elements.

## Numerical results

### *Model validation from measured displacements*

The developed model that was calibrated using site characterization data, is now validated in terms of overall stiffness by comparing the obtained numerical displacements with independent measured displacements caused by the passage of axles 15–22 from an AVE-S103 train traveling at 300 km/h (shown in Fig. 11), in terms of the average values from the three instrumented outer sections. This approach ensures that the model is not simply reproducing the input data but accurately predicting track behavior. The model of the vehicle therefore consists of eight moving axles with a mass of 1750 kg each, spaced as depicted in Fig. 10, and loaded vertically with the calculated weight per axle, in correspondence to the measured wheel loads: 53.7, 57.8, 56.0, 54.8, 58.4, 59.1, 62.6 and 64.6 kN.

Table 3 presents a comparison between measurements (Mes) and results from the numerical model (Num), exemplary for the first four axles considered, regarding rail and sleeper downward displacements, railpad vertical deformation and vertical track stiffness, denoting the good agreement between the results.

Fig. 23 depicts the agreement between the calculated vertical rail displacements at the midspan and those estimated from the field measurements (the average values presented in Fig. 11). It is seen that a closer agreement is achieved for some axles compared to others. This was expected due to the variable level of correlation between the measured peak displacements and the measured loads, as shown in Fig. 8, especially in section T23. Despite this difference, it is concluded that the developed model adequately represents the studied phenomena, providing a good agreement in terms of both the maximum downward peak displacements and the displacement profile between peaks.

Fig. 24 shows a detailed analysis of the vertical displacements along the depth of the model, together with a decomposition of the displacements per component/layer. The displacements are now taken at a

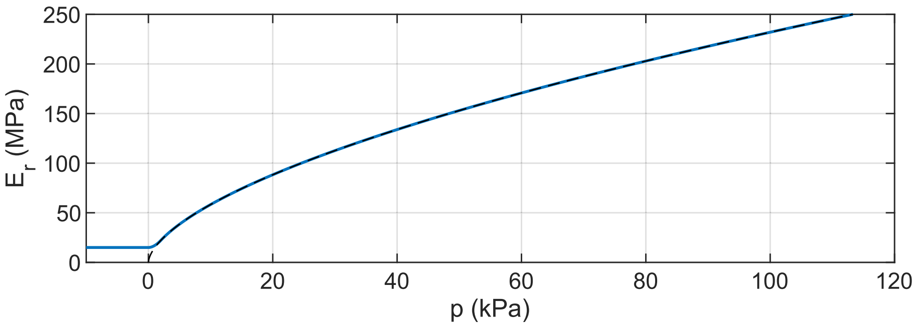

**Fig. 21.** Resilient modulus of ballast as a function of mean stress.

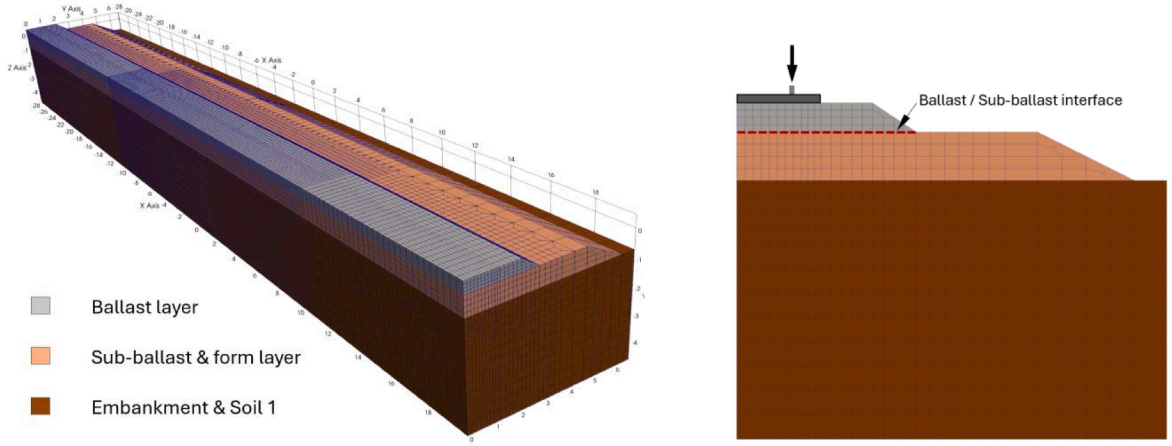

a) 3D view of the final FEM model

b) Transverse cross-section

**Fig. 22.** Views of the FEM model representing the Brihuega segment (considering symmetry) – the views show only the ballast-substructure system; dimensions in [m].

**Table 3**
Comparison between measurements and results from the numerical model; Mes – refers to the measurement (mean value); Num – refers to the result from the numerical model).

| Element/Layer | Axle15 | | Axle16 | | Axle17 | | Axle18 | |
|---|---|---|---|---|---|---|---|---|
| | Mes | Num | Mes | Num | Mes | Num | Mes | Num |
| Rail downward displacements [mm] | 0.39 | 0.39 | 0.42 | 0.41 | 0.39 | 0.40 | 0.34 | 0.40 |
| Sleeper downward displacements [mm] | 0.17 | 0.17 | 0.17 | 0.18 | 0.19 | 0.18 | 0.18 | 0.17 |
| Railpad vertical deformation [mm] | 0.17 | 0.22 | 0.15 | 0.24 | 0.15 | 0.23 | 0.16 | 0.22 |
| Vertical track stiffness [kN/mm] | 138 | 138 | 139 | 141 | 144 | 140 | 163 | 137 |

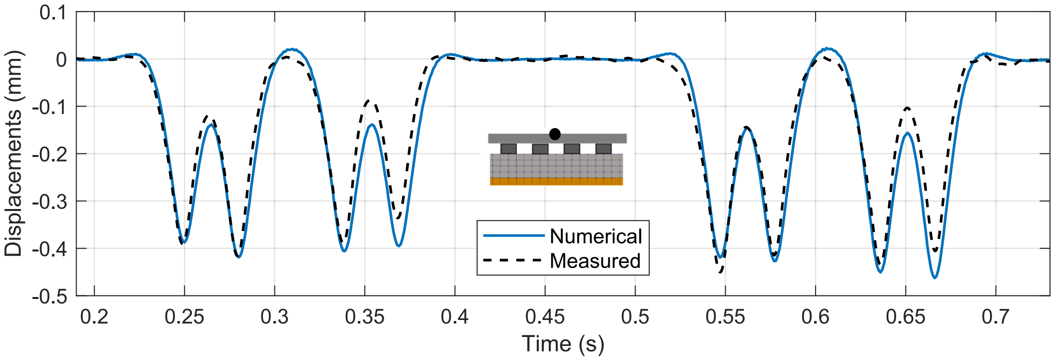

**Fig. 23.** Rail midspan vertical displacement results: comparing numerical with field measurements.

sleeper section, at locations marked in the schematic presented in the figure.

In this case, it is evident that the primary contribution to the measured rail displacements comes from the vertical deformation of the railpad (about 0.22 to 0.24 mm), followed by the deformation occurring within the ballast layer itself. This reflects the stiff nature of the track support. Additionally, the deformation at the bottom of the embankment & Soil 1 layer is very small, basically negligible, confirming that the considered model's depth is adequate for this geotechnical profile. This figure also confirms that the interpenetration between the sleepers and ballast layer as well as between the ballast and sub-ballast layers is very small, as expected.

Moreover, it is noted that the field measurements for the peak downward displacements of the sleeper (Section 2.3.3), as well as the peak vertical deformation of the railpads (Section 2.3.4), are in good agreement with the results from the numerical simulations (shown in Fig. 24), further validating the numerical model. The slightly lower measured railpad deformations may be due to higher railpad stiffness than the prescribed 100 kN/mm. This also aligns with the fact that railpad stiffness tends to increase with aging.

### *Model validation from measured accelerations*

The vertical accelerations measured in the ballast particle are compared with the accelerations calculated numerically at the corresponding position (beneath the tip of the sleeper), as shown in Fig. 25. A low-pass filter with a cut-off frequency of 175 Hz was also applied to both sets of signals. Fig. 25a, presenting the signals in the time-domain, shows that, although the results do not match perfectly – as expected – the maximum amplitudes and general response are very close. Fig. 25b depicts a strong agreement between the frequency content of the numerical and measured signals, particularly concerning harmonic

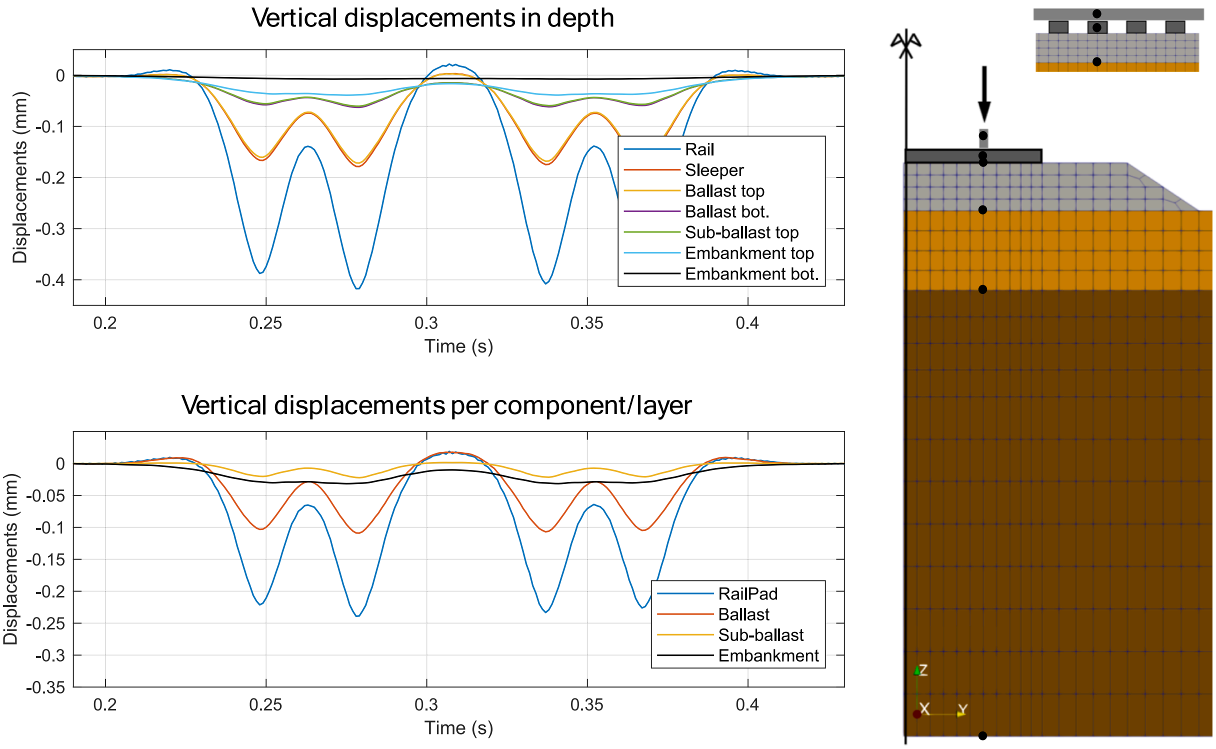

**Fig. 24.** Displacements calculated at the locations indicated in the right-hand schematic. Top left: vertical point displacements; Bottom left: vertical displacements per component/layer.

frequencies. To ensure comparability, the measured signal was down sampled to match the numerical results' sampling rate (1 kHz), and both signals were cropped to include only the segment corresponding to the two pairs of bogies (axles 15 to 22). Since this process significantly reduces the number of FFT bins, each signal was replicated three times to increase the bin count and enhance the discretization detail in the FFT plots. This approach preserves the original frequency content while allowing for more detailed analysis. It is concluded that despite representing the ballast material using a continuous approach, the numerical model captures the response at the ballast level effectively.

### *Detailed analysis of the track response*

This section presents a deeper analysis in terms of forces and stresses based on the validated 3D model, going beyond the information available from the field measurements. The analysis is focused on the results obtained for the passage of the first four axles considered in the validation section above (axles 15–18), preserving the generality of the conclusions and giving a closer detail of the analyzed variables.

### *Force transferred by the sleeper*

The total force transferred from the sleeper to the ballast layer, due to the axle loads, is depicted in Fig. 26. Based on this result, the transmissibility of the track is estimated to be about 42 % (for example for the second axle of the train model: $(52.4 - 4)/(57.8 \times 2) = 0.42$). This value aligns well with preliminary estimates derived from a Winkler model and considering a vertical track stiffness average of 146 kN/mm (see Table 3), that pointed to around 45 % of track transmissibility [16]. In Fig. 26, it is also observed that the minimum load occurs between the bogies, approaching nearly zero but without any complete loss of contact in this case.

### *Stress distribution in the track bed layers and subgrade*

Fig. 27 shows transverse and longitudinal cross-sections, with the

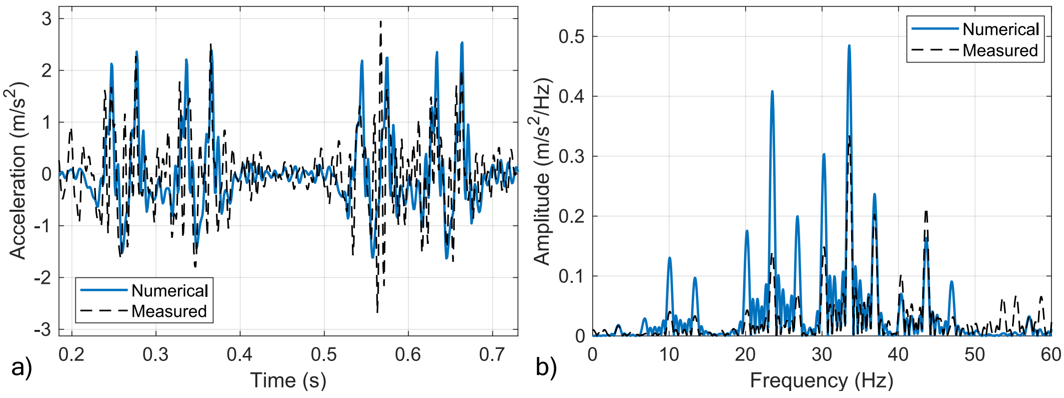

**Fig. 25.** Ballast vertical acceleration results – comparison between numerical and field measurements (low-pass filtered at 175 Hz); a) signals in the time domain; and b) frequency content.

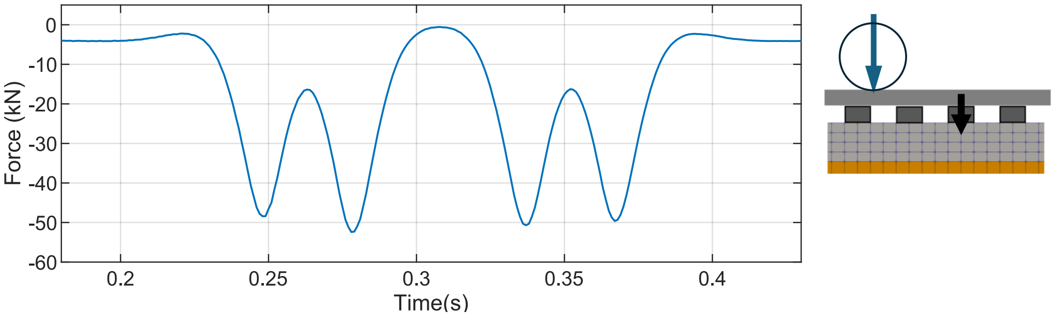

**Fig. 26.** Total force transferred from the sleeper to the ballast during train passage.

finite element mesh deformed with the nodal displacements magnified by a factor of one thousand, and where the colors refer to the stress distribution: vertical stresses ($\sigma_z$), on the left, and longitudinal stresses ($\sigma_x$), on the right. The corresponding color legends are provided in figures a) and b), ranging from $-80$ – 0 kPa for the vertical stresses and from $-30$ – 0 kPa for the horizontal stresses. The sleepers and shoulder ballast are not represented in the figures. The stress distribution in the transverse cross-sections corresponds to the moment the second axle is at the same longitudinal coordinate of these cross-sections. In these figures, it is seen that the stresses within the ballast layer vary significantly, both along the sleeper length and, as expected, with depth. The longitudinal cross-sections also show that the stress distribution is nearly symmetrical with respect to the loaded sleeper, which is indicative of a quasi-static displacement field. This is the expected scenario when the train speed is well below the shear wave velocities of the supporting track layers, as in this case. It is also clear that the cyclic stresses induced by the passage of this vehicle are generally low, far below the permissible contact pressure on the ballast bed [19]. This is due to the relatively low axle loading considered, with a maximum value of 115.6 kN.

The hydrostatic or mean stress $p$ and the deviatoric stress $q$ are important stress invariants commonly used to define loading conditions in geotechnical tests in terms of the so-called stress paths [47]. They are calculated by:

$$p = \frac{1}{3}\left(\sigma_x + \sigma_y + \sigma_z\right) \tag{8}$$

$$q = \sqrt{\frac{1}{2}\left(\left(\sigma_x - \sigma_y\right)^2 + \left(\sigma_y - \sigma_z\right)^2 + \left(\sigma_z - \sigma_x\right)^2\right) + 3\left(\tau_{xy}^2 + \tau_{yz}^2 + \tau_{zx}^2\right)} \tag{9}$$

Fig. 28 presents the time history of these stress invariants within the ballast layer during the passage of the first two axles, at four depths under the sleeper, as identified in the figure (A to D). These stresses include the geostatic field and the loading from the passing axles. It is seen that the stress increase caused by the vehicle goes well above the initial stress. The results also show that, as expected, the cyclic stress amplitudes in the ballast layer diminish with depth.

Another important parameter is the maximum $q/p$ ratio, which plays an important role in the permanent deformation of geomaterials: the higher the $q/p$ ratio, the more likely it is that unrecoverable deformation takes place. Suiker and de Borst [46] referred that the governing stress term for the development of plastic deformation through frictional sliding of granular materials, such as ballast and sub-ballast, is the cyclic ('cyc') stress ratio $(q/p)_{\text{cyc}}$. The term 'cyclic' here denotes that only the increase or amplitude from the initial geostatic condition and caused by the passing vehicle is considered, as denoted in Fig. 28(a). From cyclic densification tests performed in fresh ballast, and following the shakedown theory, Suiker identified three possible deformation regimes depending on the maximum $(q/p)_{\text{cyc}}$ reached, namely (i) $(q/p)_{\text{cyc}} \le h_0$, which corresponds to an elastic regime, (ii) $h_0 < (q/p)_{\text{cyc}} \le h_m$, which corresponds to a plastic response that turns into an elastic shakedown after a given number of load cycles and (iii) $(q/p)_{\text{cyc}} > h_m$, which

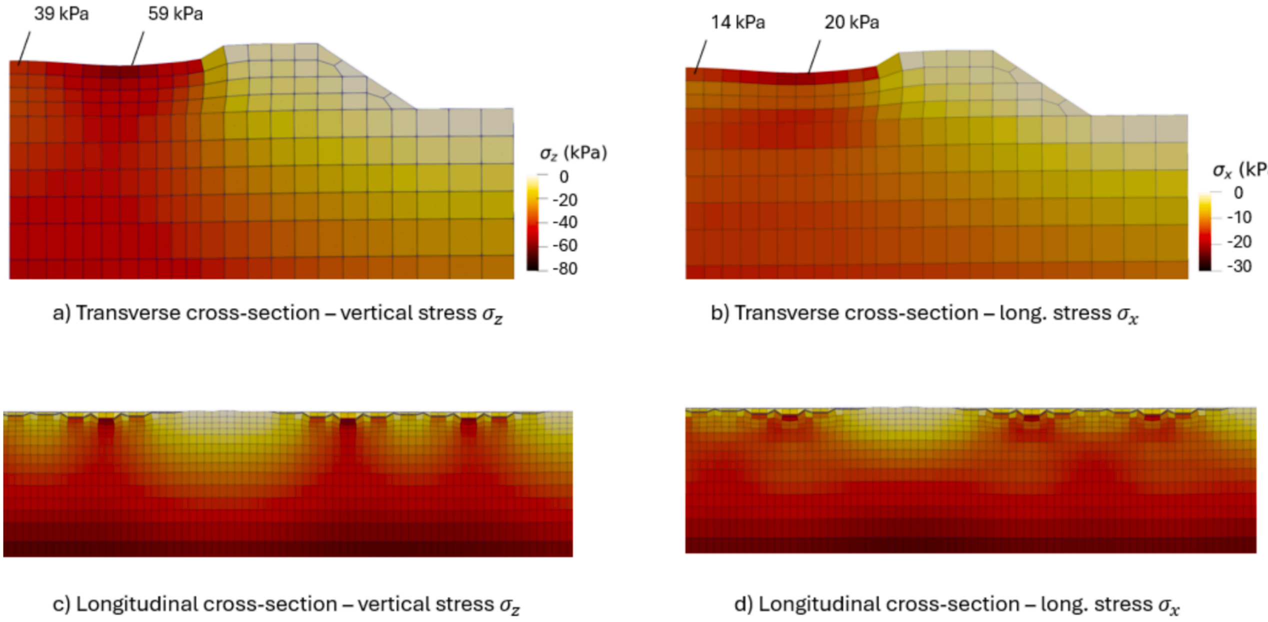

a) Transverse cross-section – vertical stress $\sigma_z$

b) Transverse cross-section – long. stress $\sigma_x$

c) Longitudinal cross-section – vertical stress $\sigma_z$

d) Longitudinal cross-section – long. stress $\sigma_x$

**Fig. 27.** Views of the vertical stress distribution in the track bed layers and subgrade when loaded by the train and the gravity field, superimposed on the deformed track (displacements magnified 1000x).

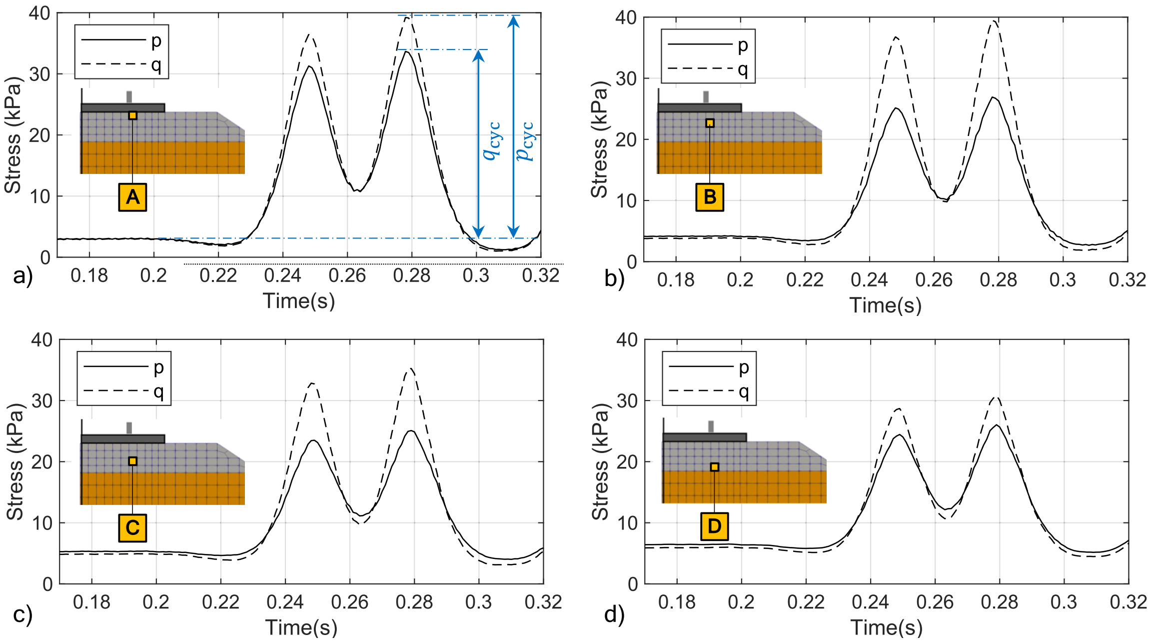

**Fig. 28.** Time history of mean stress ($p$) and deviatoric stress ($q$) at four locations within the ballast layer (A, B, C and D).

corresponds to a plastic response that progressively and continuously increases with the number of load cycles.

Fig. 29 presents the $(q/p)_{cyc}$ calculated for the case presented and for the same four locations (identified in Fig. 28). It is possible to observe that the $(q/p)_{cyc}$ ratio generally increases with the passing of the train, reaching higher values in the middle of the ballast layer (locations B and C), but not exceeding 1.5. As a reference, the triaxial tests made by Suiker identified $h_0 = 0.5$ and $h_m = 1.85$ for the tested ballast material.

The higher $(q/p)_{cyc}$ ratio reached in the middle of the ballast layer (locations B and C) can be explained if analyzing the ballast confinement. Fig. 30 depicts the horizontal confinement, showing in a color map the longitudinal stress distribution in the upper layers of the track, being similar to Fig. 27(d). It is seen that the greater horizontal stresses are found right under the sleeper base, in the ballast between the sleepers, and in the interface between the ballast and the sub-ballast. This is in part a consequence of the greater confinement provided by the contacting surfaces: the concrete sleeper above and the stiff sub-ballast below. Higher confinement leads to higher hydrostatic stress ($p$), and therefore to a lower $q/p$ ratio, thus explaining the observation made above.

A closer inspection of the ballast/sub-ballast interface in Fig. 30 also reveals that no noticeable sliding is taking place at this interface (this is, in fact, in the order of $10^{-6}$ m). This aspect is a natural consequence of considering reasonably high contact stiffness values and a high friction coefficient (0.65). It can be stated that for dynamic analyses aimed at calculating the stress-displacement field due to passing trains in normal (stiff) ballast/sub-ballast contact, the shared node approach seems to be an adequate and simpler option. However, in comparative analysis, some small differences (up to 8 %) were found, in terms of stresses in the interface elements. Nevertheless, this condition does not account for, e.g., the presence of a geotextile between these two layers, which would reduce the friction coefficient. Also, this conclusion excludes analyses aimed at evaluating long-term ballast deformation, for which the more realistic Coulomb friction interface is likely a better option.

To better understand how the stress invariants vary under the sleeper, Fig. 31 presents the maximum values of $p_{cyc}$, $q_{cyc}$, and $(q/p)_{cyc}$ when the second (heaviest) axle is located above the presented sleeper, on a transverse cross-section view. It is seen that the maximum values of $p_{cyc}$ and $q_{cyc}$ are attained right under the rail and that these amplitudes rapidly diminish with depth. Regarding the $(q/p)_{cyc}$ ratio, the maximum values are reached in the ballast layer under the tip of the sleeper, but considerably high values are also found inside the sub-ballast layer, although where the mean stress increase $p_{cyc}$ is much lower. It is also visible that the maximum ratio stays below 1.85, which indicates that, as explained above, for this loading condition the expected plastic deformation in the ballast is small and tends to a stable shakedown limit [47]. It is however mentioned that this ratio will tend to increase with the

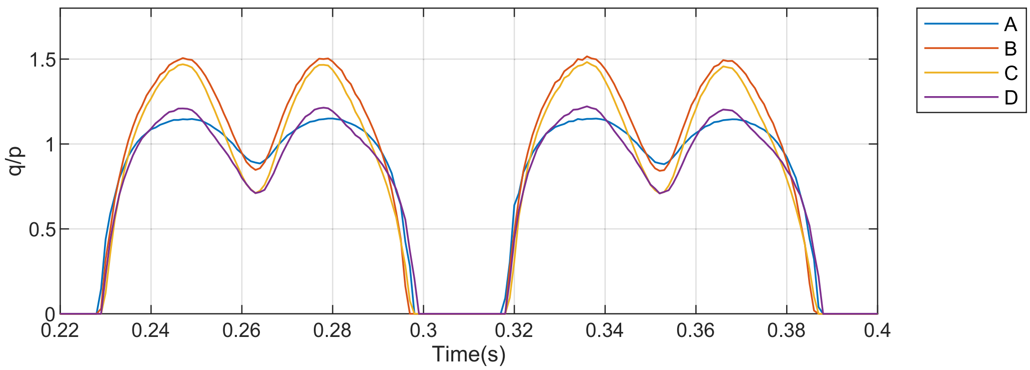

**Fig. 29.** Time history of $(q/p)_{cyc}$ ratio at four locations within the ballast layer (A, B, C and D).

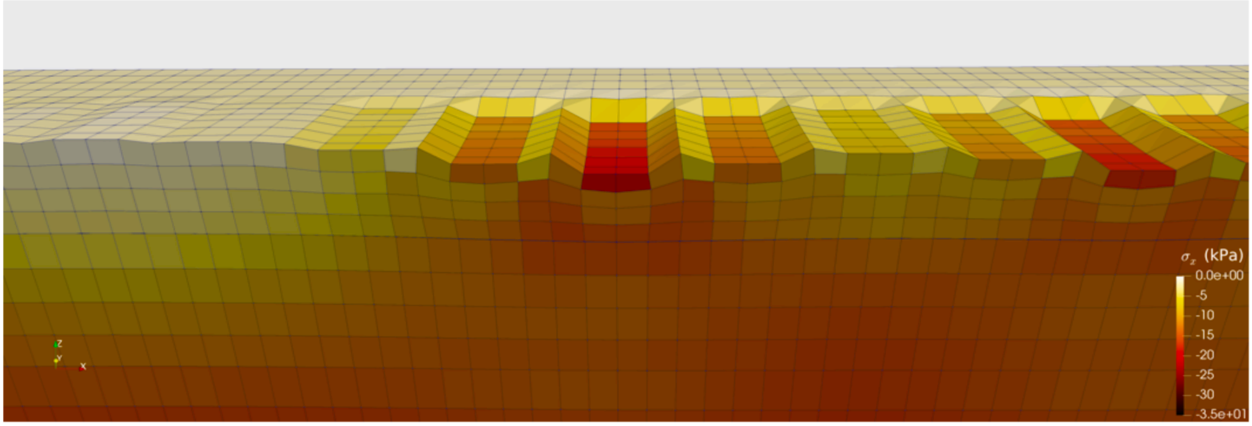

**Fig. 30.** Longitudinal cross-section under the rail showing the track bed layers FEM mesh deformed by instant nodal displacements (amplified 1000x) and the colors relative to the longitudinal stress $\sigma_x$.

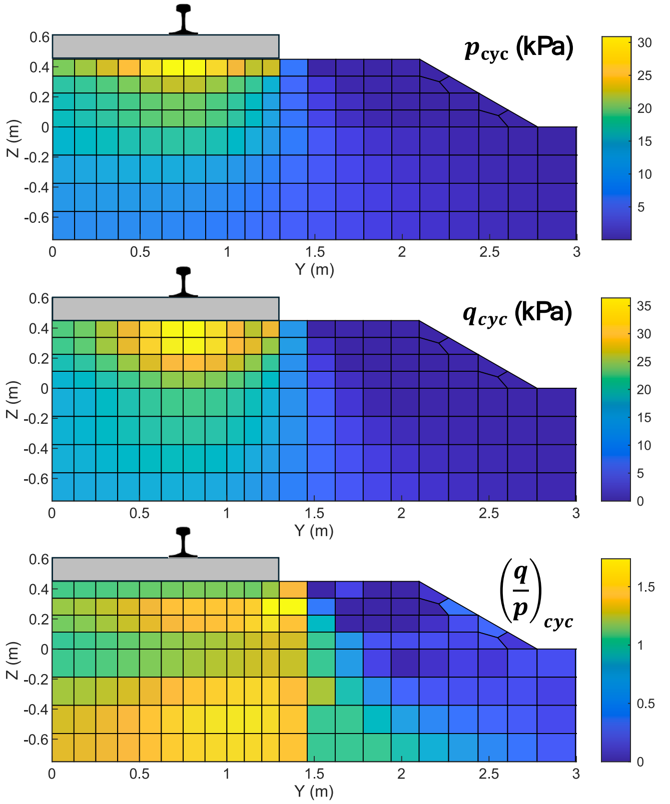

**Fig. 31.** Distribution of the maximum $p_{cyc}$, $q_{cyc}$, and $(q/p)_{cyc}$ ratio in a transverse cross-section.

consideration of irregularities and non-uniformities in the model, that were left aside from this study.

### Railpad stiffness reduction

This section investigates the effect of reducing the railpad stiffness. To this purpose, a new simulation with a railpad stiffness of 60 kN/mm was performed, to compare with the results presented above, obtained with a railpad stiffness of 100 kN/mm. The aim is to clarify if this stiffness reduction may improve the railway track response in the long-term, decreasing ballast degradation and its plastic deformation.

Concerning the track displacements, as seen in Fig. 32, the softer railpad leads to an increase of the rails displacements, as expected, but to a slight reduction of the downward sleeper displacement. At the base of the ballast layer, and below, the differences are minimal. The vertical track stiffness decreases from 139 kN/mm to 109 kN/mm, resulting in a significant 21 % reduction.

The track stiffness reduction promotes a higher distribution of forces through the sleepers. This is seen in Fig. 33, depicting again the total force transmitted through the sleeper, where it is seen the beneficial effect obtained with the softer railpad, by reducing the maximum sleeper force by 9 %, due to a lower transmissibility of the track (which, e.g., for the first axle decreased from 41.3 % to 37.6 %).

Most notably, reducing the railpad stiffness positively decreases the level of ballast vibration caused by high-speed trains. This effect is illustrated in Fig. 34, which presents the calculated accelerations in the ballast particle beneath the tip of the sleeper, comparing the response obtained with the two railpad stiffness values. The vibration level reduction is approximately 25 % in terms of amplitude. This decrease promotes reduced ballast wear and abrasion, minimizing settlements and extending the ballast layer service life.

Fig. 35 shows the stress distribution in the ballast layer, in terms of vertical stresses (left) and longitudinal stresses (right), calculated for the two railpad stiffness values. The vertical stresses generally decrease beneath the sleepers with lower railpad stiffness, particularly in the upper elements, due to reduced transmissibility. However, the horizontal stress confinement, while slightly reduced, is less significantly affected. This stress reduction is also beneficial to the ballast particles, as it mitigates wear, abrasion, and breakage.

The stress reduction in the ballast layer induced by the softer railpad is further demonstrated in terms of the stress invariants $p$ and $q$ (relative to total stresses), as shown in Fig. 36. Reducing the railpad stiffness from 100 kN/mm to 60 kN/mm results in a maximum deviatoric stress ($q$) reduction of about 10 %, and a maximum mean stress ($p$) reduction of about 8 %. This difference can be explained with the results in Fig. 35: when the reduction in vertical stress is greater than the reduction in horizontal confinement, the deviatoric stress reduction naturally exceeds the mean stress reduction.

Consequently, the cyclic stress ratio $(q/p)_{cyc}$ will also follow a beneficial reduction trend, as shown in Fig. 37 for the same two ballast locations (A and B), corresponding to a loading condition within the ballast layer during train passages that is less prone to particle degradation and to plastic deformations.

The investigation on reducing railpad stiffness demonstrated that softer railpads (60 kN/mm) can lead to notable changes in ballast response. While the softer railpads resulted in increased rail displacements and a subsequent decrease in overall track stiffness (around 20 %). They also led to a slight reduction in sleeper displacement. The track stiffness reduction promoted a more even distribution of forces across

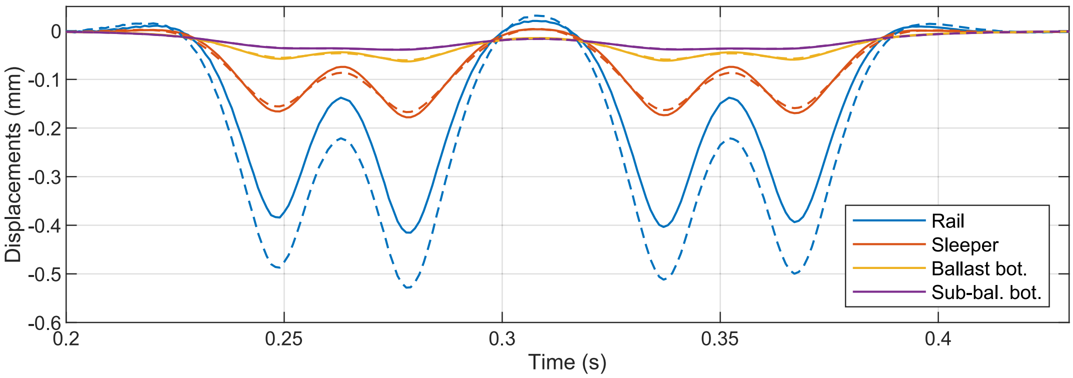

**Fig. 32.** Point vertical displacements in the rail, the sleeper, at the base of the ballast layer and at the base of the sub-ballast layer. Solid lines: Railpad 100 kN/mm; Dashed lines: Railpad 60 kN/mm.

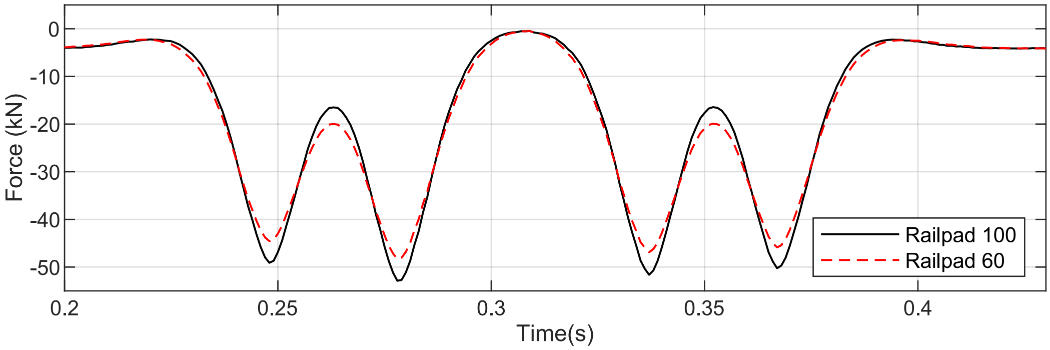

**Fig. 33.** Total force transferred from the sleeper to the ballast with railpads of 100 kN/mm and 60 kN/mm.

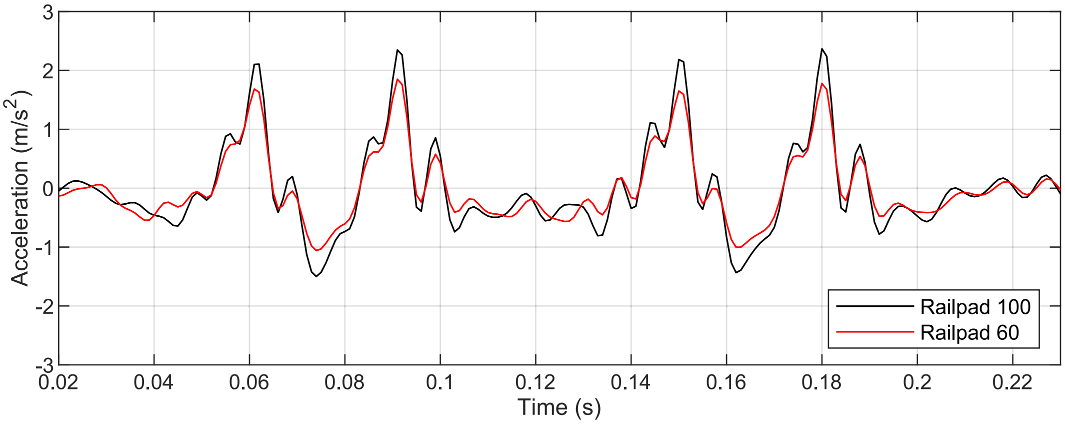

**Fig. 34.** Ballast vertical acceleration results: comparing numerical response with railpads of 100 kN/mm and 60 kN/mm.

sleepers, lowering the peak force transferred from each sleeper to the ballast layer by about 10 %. Additionally, the lower vertical stresses in the ballast layer, especially under the sleeper bases, are beneficial for reducing particle wear, abrasion, and breakage within the ballast, potentially extending track lifespan [26]. These findings suggest that adopting railpads with lower stiffness could be a viable strategy to mitigate ballast degradation in high-speed rail tracks, providing an important consideration for maintenance and future design adjustments to enhance track resilience and longevity. Notwithstanding, the authors acknowledge that altering the vertical stiffness of the railpads (and, consequently, the track) may introduce additional challenges that could influence the overall performance of the railway system. Examples of this are increased train energy consumption and higher rail bending fatigue, which were deemed beyond the scope of this study.

## Conclusions

This study explored the dynamic behavior of ballasted railway tracks during high-speed train passages through field measurements and advanced numerical modeling. The key findings are summarized as follows:

1. Field Measurements:
    - The Brihuega railway segment exhibited significant dynamic ballast responses at the current maximum Spanish high-speed network (300 km/h). The ballast displayed resilient behavior, with temporary deformations recovering after train passages, as expected.

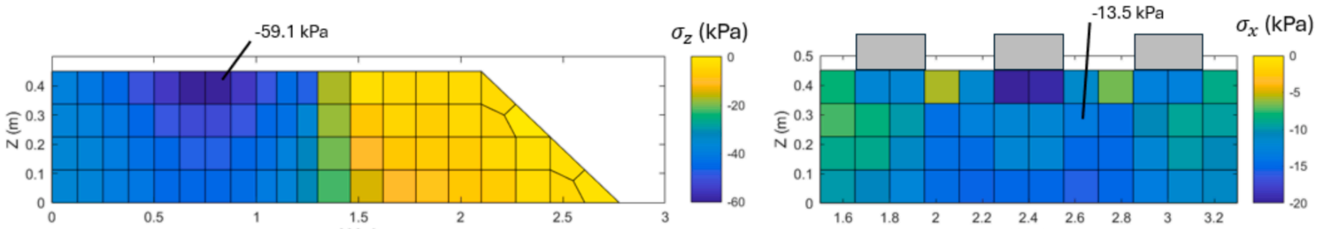

a) Railpad = 100 kN/mm

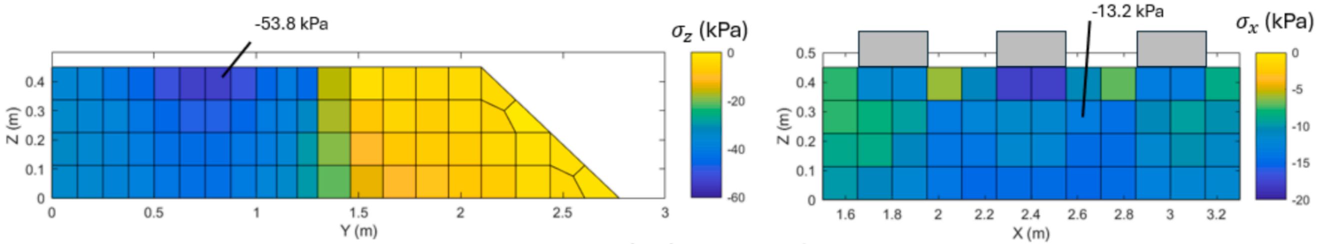

b) Railpad = 60 kN/mm

**Fig. 35.** Vertical stress distribution in a transverse cross-section under the sleeper. Upper figures: results with railpad of 100 kN/mm; Bottom figures: results with railpad of 60 kN/mm.

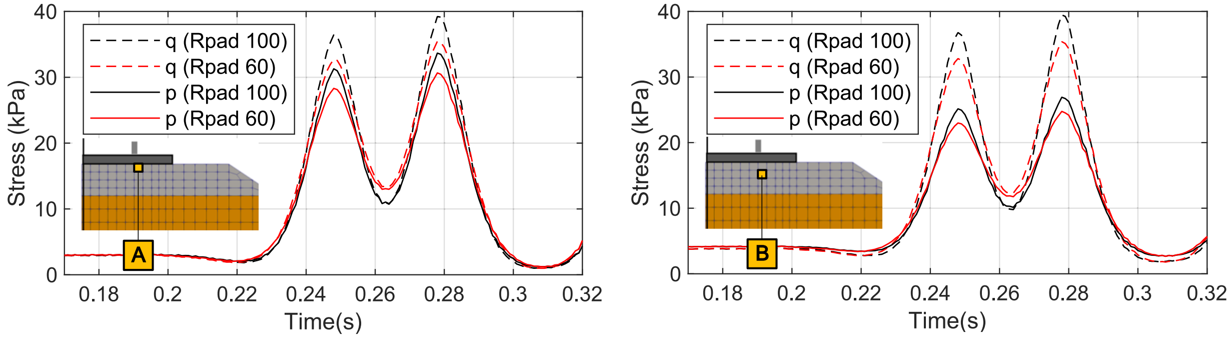

**Fig. 36.** Time history of total $p$ and $q$ at two locations within the ballast layer: comparing numerical response with railpads of 100 kN/mm and 60 kN/mm.

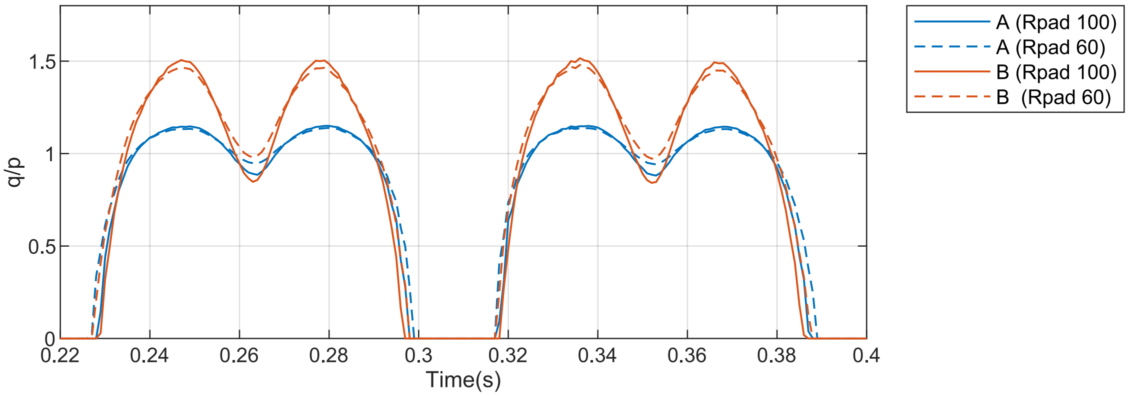

**Fig. 37.** Time history of $(q/p)_{\text{cyc}}$ ratio at two locations within the ballast layer (A and B): comparing numerical response with railpads of 100 kN/mm and 60 kN/mm.

- Variability in measured loads and displacements was attributed to rail and wheel irregularities, uneven track support conditions, and measurement uncertainties.

2. Numerical modeling:
    - A validated 3D model accurately replicated field-measured vertical displacements, among other aspects, confirming its robustness in simulating dynamic train-track-substructure interactions.
    - Elastic deformation primarily occurred in the railpads and ballast, with deeper layers largely unaffected. Stress paths within the ballast layer aligned with observed moderate ballast degradation.
    - Non-linear Coulomb friction modeling at sleeper-ballast and ballast/sub-ballast interfaces captured realistic stress transfers, showing minimal sliding at these layers.
3. Impact of railpad stiffness reduction from 100 kN/mm to 60 kN/mm:
    - Softer railpads reduced peak ballast stresses by 10 %, distributed forces more evenly across sleepers, and lowered vertical stresses,

mitigating ballast wear and prolonging ballast service life. Rail displacement increased, reducing overall track stiffness by 20 %.

4. Limitations and Future Work:
   - The model assumes uniform track conditions and does not consider cumulative loading effects. Future research should include variable support conditions and long-term load simulations to better assess track durability under high-speed traffic.

Despite these limitations, the validated 3D model offers a versatile tool for railway engineering, enabling detailed analysis of dynamic interactions and the prediction of critical parameters that are otherwise difficult or impossible to measure directly in-situ, such as stress distributions, subsurface vibrations, and critical speeds for HSL.

## CRediT authorship contribution statement

**José Nuno Varandas:** Writing – review & editing, Writing – original draft, Visualization, Validation, Supervision, Software, Resources, Methodology, Investigation, Conceptualization. **André Paixão:** Writing – review & editing, Visualization, Validation, Methodology, Investigation, Conceptualization. **Ángel Tijera:** Writing – review & editing, Visualization, Validation, Resources, Methodology, Investigation, Conceptualization. **Inés Crespo-Chacón:** Writing – review & editing, Visualization, Validation, Resources, Methodology, Investigation, Conceptualization. **José Estaire:** Writing – review & editing, Validation, Supervision, Resources, Methodology, Investigation, Conceptualization. **Eduardo Fortunato:** Writing – review & editing, Supervision, Methodology, Investigation, Conceptualization.

## Declaration of competing interest

The authors declare that they have no known competing financial interests or personal relationships that could have appeared to influence the work reported in this paper.

## Acknowledgements

The authors express their gratitude to ADIF for granting the necessary permissions and providing support to conduct the in-situ measurements presented in this work.

## Data availability

Data will be made available on request.

## References

[1] Abadi T, Pen LL, Zervos A, Powrie W. Improving the performance of railway tracks through ballast interventions. Proc Inst Mech Eng F J Rail Rapid Transit 2018;232 (2):337–55. https://doi.org/10.1177/0954409716671545.
[2] Alabbasi Y, Hussein M. Geomechanical modelling of railroad ballast: a review. Arch Comput Meth Eng 2021;28(3):815–39. https://doi.org/10.1007/s11831-019-09390-4.
[3] Alves Costa P, Calçada R, Cardoso A. Track-ground vibrations induced by railway traffic: in-situ measurements and validation of a 2.5D FEM-BEM model. Soil Dyn Earthq Eng 2012;32(1):111–28.
[4] Alves Costa P, Calçada R, Cardoso AS, Bodare A. Influence of soil non-linearity on the dynamic response of high-speed railway tracks. Soil Dyn Earthq Eng 2010;30 (4):221–35. https://doi.org/10.1016/j.soildyn.2009.11.002.
[5] Alves Fernandes V. Numerical analysis of nonlinear soil behavior and heterogeneity effects on railway track response (Issue 2014ECAP0055) [Ecole Centrale Paris]; 2014. https://theses.hal.science/tel-01127387.
[6] Alves Ribeiro C, Calçada R, Delgado R. Experimental assessment of the dynamic behaviour of the train-track system at a culvert transition zone. Eng Struct 2017; 138:215–28. https://doi.org/10.1016/j.engstruct.2017.02.020.
[7] Anbazhagan P, Buddhima I, Amarajeevi G. Characterization of clean and fouled rail track ballast subsurface using seismic surface survey method: model and field studies. J Test Eval 2011;39(5):831–41. https://doi.org/10.1520/JTE103472.
[8] Aursudkij B, McDowell GR, Collop AC. Cyclic loading of railway ballast under triaxial conditions and in a railway test facility. Granul Matter 2009;11:391–401. https://doi.org/10.1007/s10035-009-0144-4.
[9] Baessler M, Ruecker W. Track settlement due to cyclic loading with low minimum pressure and vibrations. System dynamics and long-term behaviour of railway vehicles, track and subgrade. Springer; 2003.
[10] Barbosa JMde O, Fărăgău AB, van Dalen KN, Steenbergen MJMM. Modelling ballast via a non-linear lattice to assess its compaction behaviour at railway transition zones. J Sound Vib 2022;530. https://doi.org/10.1016/j.jsv.2022.116942.
[11] Bian X, Jiang J, Jin W, Sun D, Li W, Li X. Cyclic and postcyclic triaxial testing of ballast and subballast. J Mater Civ Eng 2016;28(7). https://doi.org/10.1061/(asce)mt.1943-5533.0001523.
[12] Bian X, Li W, Qian Y, Tutumluer E. Analysing the effect of principal stress rotation on railway track settlement by discrete element method. Geotechnique 2020;70(9): 803–21. https://doi.org/10.1680/jgeot.18.P.368.
[13] Coelho B, Priest J, Hölscher P, Powrie W. Monitoring of transition zones in railways; 2009.
[14] Cundall PA, Strack ODL. A discrete numerical model for granular assemblies. Géotechnique 1979;29(1):47–65. https://doi.org/10.1680/geot.1979.29.1.47.
[15] de Melo ALO, Kaewunruen S, Papaelias M. Effect of unsupported sleepers on vertical levelling loss of heavy-haul railway track geometry under cyclic loadings. Civil Eng Metall Mater 2024;238(10):1199–211. https://doi.org/10.1177/09544097241266289.
[16] Estaire J, Crespo-Chacón I. Determining the railway critical speed by using static FEM calculations. Num Meth Geotech Eng IX 2018;2:1587–96. https://doi.org/10.1201/9780429446924-86.
[17] Estaire J, Moreno J, Pardo de Santayana F, Santana M. Activities of the Laboratorio de Geotecnia-CEDEX related to railway geotechnical engineering (in Spanish). Ingeniería Civil 2022;200:49–72. https://ingenieriacivil.cedex.es/index.php/ingenieria-civil/article/view/2464.
[18] Estaire J, Santana M. Large Direct Shear Tests Performed with Fresh Ballast. ASTM Spec Tech Publ STP 2018;1605:144–61. https://doi.org/10.1520/STP160520170137.
[19] Esveld C. Modern railway track. (2nd ed.). MRT-Productions; 2001.
[20] Fernández-Ruiz J, Castanheira-Pinto A, Costa PA, Connolly DP. Influence of non-linear soil properties on railway critical speed. Constr Build Mater 2022;335. https://doi.org/10.1016/j.conbuildmat.2022.127485.
[21] Guo Y, Zhao C, Markine V, Shi C, Jing G, Zhai W. Discrete element modelling of railway ballast performance considering particle shape and rolling resistance. Railway Eng Sci 2020;28(4):382–407. https://doi.org/10.1007/s40534-020-00216-9.
[22] Hu G, Hu Z, Jian B, Liu L, Wan H. On the determination of the damping coefficient of non-linear spring-dashpot system to model hertz contact for simulation by discrete element method. In: 2010 WASE international conference on information engineering, Vol. 3; 2010. p. 295–8.
[23] Indraratna B, Ionescu D, Christie HD. Shear behavior of railway ballast based on large-scale triaxial tests. J Geotech and Geoenvir Engrg 1998;124(5):439–49. https://doi.org/10.1061/(ASCE)1090-0241(1998)124:5(439).
[24] Indraratna B, Nimbalkar S, Christie D, Rujikiatkamjorn C, Vinod J. Field assessment of the performance of a ballasted rail track with and without geosynthetics. J Geotech Geoenviron Eng 2010;136(7):907–17. https://doi.org/10.1061/(ASCE)GT.1943-5606.0000312.
[25] Ishibashi I, Zhang X. Unified dynamic shear moduli and damping ratios of sand and clay. Soils Found 1993;33(1):182–91. https://doi.org/10.3208/sandf1972.33.182.
[26] Jayasuriya C, Indraratna B, Ngoc Ngo T. Experimental study to examine the role of under sleeper pads for improved performance of ballast under cyclic loading. Transp Geotech 2019;19:61–73. https://doi.org/10.1016/J.TRGEO.2019.01.005.
[27] Jing G, Ding D, Liu X. High-speed railway ballast flight mechanism analysis and risk management – A literature review. Constr Build Mater 2019;223:629–42. https://doi.org/10.1016/J.CONBUILDMAT.2019.06.194.
[28] Kouroussis G, Connolly DP, Verlinden O. Railway-induced ground vibrations – a review of vehicle effects. Int J Rail Transp 2014;2(2):69–110. https://doi.org/10.1080/23248378.2014.897791.
[29] Lackenby J, Indraratna B, McDowell G, Christie D. Effect of confining pressure on ballast degradation and deformation under cyclic triaxial loading. Geotechnique 2007;57(6):527–36.
[30] Lekarp F, Isacsson U, Dawson A. State of the art. I: resilient response of unbound aggregates. J Transp Eng 2000;126(1):66–75. https://doi.org/10.1061/(ASCE)0733-947X(2000)126:1(66).
[31] Lim WL, McDowell GR. Discrete element modelling of railway ballast. Granul Matter 2005;7(1):19–29. https://doi.org/10.1007/s10035-004-0189-3.
[32] Lu M, McDowell G. The importance of modelling ballast particle shape in the discrete element method. Granul Matter 2007;9(1):69–80.
[33] Marolt Čebašek T, Esen AF, Woodward PK, Laghrouche O, Connolly DP. Full scale laboratory testing of ballast and concrete slab tracks under phased cyclic loading. Transp Geotech 2018;17:33–40. https://doi.org/10.1016/j.trgeo.2018.08.003.
[34] McDowell GR, Lim WL, Collop AC, Armitage R, Thom NH. Laboratory simulation of train loading and tamping on ballast. Proc Inst Civil Eng - Transp 2005;158(2): 89–95. https://doi.org/10.1680/tran.2005.158.2.89.
[35] Mezher SB, Connolly DP, Woodward PK, Laghrouche O, Pombo J, Costa PA. Railway critical velocity - Analytical prediction and analysis. Transp Geotech 2016; 6:84–96. https://doi.org/10.1016/j.trgeo.2015.09.002.
[36] Moreno J, García de la Oliva JL. Determinación de las cargas aplicadas al carril mediante bandas extensométricas (in Spanish). Ingeniería Civil 2012;165:123–9. https://ingenieriacivil.cedex.es/index.php/ingenieria-civil/article/view/272.
[37] Olivier B, Verlinden O, Kouroussis G. A vehicle/track/soil model using co-simulation between multibody dynamics and finite element analysis. Int J Rail Transp 2020;8(2):135–58. https://doi.org/10.1080/23248378.2019.1642152.

[38] Paixão A. Transition zones in railway tracks. An experimental and numerical study on the structural behaviour. Faculty of Engineering of University of Porto; 2014.

[39] Paixão A, Varandas JN, Fortunato E, Calçada R. Numerical simulations to improve the use of under sleeper pads at transition zones to railway bridges. Eng Struct 2018;164:169–82. https://doi.org/10.1016/j.engstruct.2018.03.005.

[40] Quintanilla I. Multi-scale study of the degradation of railway ballast [PhD]. Université Grenoble Alpes; 2018.

[41] Ramos A, Gomes Correia A, Calçada R, Alves Costa P, Esen A, Woodward PK, et al. Influence of track foundation on the performance of ballast and concrete slab tracks under cyclic loading: physical modelling and numerical model calibration. Constr Build Mater 2021;277. https://doi.org/10.1016/j.conbuildmat.2021.122245.

[42] Santana M, Estaire J. Test results of friction resistance in the sleeper – ballast contact. Proceedings of the XVII ECSMGE-2019. 2019.

[43] Schmitt L. Recent SNCF research on ballasted high speed track. Fatigue behaviour. Track for High-Speed Railways; 2006.

[44] Shaer AA, Duhamel D, Sab K, Foret G, Schmitt L. Experimental settlement and dynamic behavior of a portion of ballasted railway track under high speed trains. J Sound Vib 2008;316(1–5):211–33. https://doi.org/10.1016/j.jsv.2008.02.055.

[45] Shih J-Y, Grossoni I, Bezin Y. Settlement analysis using a generic ballasted track simulation package. Transp Geotech 2019;20:100249. https://doi.org/10.1016/j.trgeo.2019.100249.

[46] Suiker ASJ, de Borst R. A numerical model for the cyclic deterioration of railway tracks. Int J Numer Meth Eng 2003;57(4):441–70. https://doi.org/10.1002/nme.683.

[47] Suiker ASJ, Selig ET, Frenkel R. Static and cyclic triaxial testing of ballast and subballast. J Geotech Geoenviron Eng 2005;131(6):771–82. https://doi.org/10.1061/(ASCE)1090-0241(2005)131:6(771).

[48] Takemiya H. Simulation of track-ground vibrations due to a high-speed train: the case of X-2000 at Ledsgard. J Sound Vib 2003;261(3):503–26. https://doi.org/10.1016/S0022-460X(02)01007-6.

[49] Tijera A, Ruiz R, Cuellár V, Rodriguéz M. Track stiffness variations in transition zones (in Spanish). Ingeniería Civil 2012;165:103–12. https://ingenieriacivil.cedex.es/index.php/ingenieria-civil/article/download/270/255/.

[50] Tutumluer E, Qian Y, Hashash YMA, Ghaboussi J, Davis DD. Discrete element Modelling of ballasted track deformation Behaviour. Int J Rail Transp 2013;1(1):57–73. https://doi.org/10.1080/23248378.2013.788361.

[51] Varandas JN. Long-term behaviour of railways transitions under dynamic loading. Application to soft soil sites. Universidade Nova de Lisboa; 2013.

[52] Varandas JN, Hölscher P, Silva MAG. Three-dimensional track-ballast interaction model for the study of a culvert transition. Soil Dyn Earthq Eng 2016;89:116–27. https://doi.org/10.1016/j.soildyn.2016.07.013.

[53] Varandas JN, Paixão A, Fortunato E. A study on the dynamic train-track interaction over cut-fill transitions on buried culverts. Comput Struct 2017;189:49–61. https://doi.org/10.1016/j.compstruc.2017.04.017.

[54] Varandas JN, Paixão A, Fortunato E, Hölscher P. A numerical study on the stress changes in the ballast due to train passages. Procedia Eng 2016;143. https://doi.org/10.1016/j.proeng.2016.06.127.

[55] Varandas JN, Paixão A, Fortunato E, Zuada Coelho B, Hölscher P. Long-term deformation of railway tracks considering train-track interaction and non-linear resilient behaviour of aggregates-a 3D FEM implementation. Comput Geotech 2020;126. https://doi.org/10.1016/j.compgeo.2020.103712.

[56] Wang H, Chang L, Markine V. Structural health monitoring of railway transition zones using satellite radar data. Sensors 2018;18(2):413. https://doi.org/10.3390/S18020413.

[57] Zhai WM. Two simple fast integration methods for large-scale dynamic problems in engineering. Int J Numer Meth Eng 1996;39(24):4199–214.